



## 3D printing of conch-like scaffolds for guiding cell migration and directional bone growth

Boshi Feng<sup>a,b</sup>, Meng Zhang<sup>a,b</sup>, Chen Qin<sup>a,b</sup>, Dong Zhai<sup>a</sup>, Yufeng Wang<sup>a</sup>, Yanling Zhou<sup>a,b</sup>, Jiang Chang<sup>a,b</sup>, Yufang Zhu<sup>a,b</sup>, Chengtie Wu<sup>a,b,\*</sup>

<sup>a</sup> State Key Laboratory of High Performance Ceramics and Superfine Microstructure, Shanghai Institute of Ceramics Chinese Academy of Sciences, Shanghai, 200050, People's Republic of China

<sup>b</sup> Center of Materials Science and Optoelectronics Engineering, University of Chinese Academy of Sciences, Beijing, 100049, People's Republic of China

### ARTICLE INFO

#### Keywords:

3D printing  
Spiral structure  
Conch-like scaffolds  
Cell migration  
Tissue regeneration  
Severe bone defects

### ABSTRACT

Regeneration of severe bone defects remains an enormous challenge in clinic. Developing regenerative scaffolds to directionally guide bone growth is a potential strategy to overcome this hurdle. Conch, an interesting creature widely spreading in ocean, has tough spiral shell that can continuously grow along the spiral direction. Herein, inspired by the physiological features of conches, a conch-like (CL) scaffold based on  $\beta$ -TCP bioceramic material was successfully prepared for guiding directional bone growth *via* digital light processing (DLP)-based 3D printing. Benefiting from the spiral structure, the CL scaffolds significantly improved cell adhesion, proliferation and osteogenic differentiation *in vitro* compared to the conventional 3D scaffolds. Particularly, the spiral structure in the scaffolds could efficiently induce cells to migrate from the bottom to the top of the scaffolds, which was like “cells climbing stairs”. Furthermore, the capability of guiding directional bone growth for the CL scaffolds was demonstrated by a special half-embedded femoral defects model in rabbits. The new bone tissue could consecutively grow into the protruded part of the scaffolds along the spiral cavities. This work provides a promising strategy to construct biomimetic biomaterials for guiding directional bone tissue growth, which offers a new treatment concept for severe bone defects, and even limb regeneration.

### 1. Introduction

Annually, over 20 million individuals worldwide suffer from bone defects causing by bone diseases, aging population, accidents, etc [1]. Due to the severe bone nonunion and limited self-healing ability of bone tissue [2,3], the regeneration of severe bone defects, such as segmental bone defects and severed limbs [4–7], remains an enormous challenge in clinic [8–11]. For severe bone defects, the distal part seriously lacks in osteogenic environment and active cells for regenerating new bone [12]. It is of great importance for the implanted scaffolds to induce cells migrating from proximal part to distal part in a well-ordered manner, and thereby to achieve directional bone growth. 3D printing of bone tissue engineering scaffolds has been demonstrated to be an efficient candidate for treating large bone defects [13–15]. Nevertheless, most of conventional scaffolds prepared by 3D printing are crossly stacked by simple solid struts [16,17]. Although being porous, they still lack a

suitable structure to guide bone cells to directionally migrate and improve the transmission of nutrients in scaffolds [18–26], resulting in the limited osteogenesis in center and distal part of the defects [27]. Thus, the structure of the 3D-printed scaffolds needs to be ingeniously designed to break through these limitations.

After millions of years of evolution, many creatures in nature have evolved wonderful physiological structures and functions [28–32]. Conches, which widely spread in ocean, generally possess a distinctive spiral structure [33,34]. The spiral conch shells with excellent mechanical properties, can perfectly support and protect the living soft tissues inside conch, and allow them to move freely and smoothly in the spiral cavity. Notably, the spiral shells can continue to grow epitaxially along the spiral direction in the whole lifecycle of conch [33]. Similarly, ideal scaffolds are expected to possess the function for guiding and promoting the new bone to continuously regenerate from the proximal part to the distal part. Therefore, the interesting features of conches

Peer review under responsibility of KeAi Communications Co., Ltd.

\* Corresponding author. State Key Laboratory of High Performance Ceramics and Superfine Microstructure, Shanghai Institute of Ceramics, Chinese Academy of Sciences, 1295 Dingxi Road, Shanghai, 200050, People's Republic of China.

E-mail address: [chentiewu@mail.sic.ac.cn](mailto:chentiewu@mail.sic.ac.cn) (C. Wu).

<https://doi.org/10.1016/j.bioactmat.2022.09.014>

Received 9 July 2022; Received in revised form 9 September 2022; Accepted 15 September 2022

2452-199X/© 2022 The Authors. Publishing services by Elsevier B.V. on behalf of KeAi Communications Co. Ltd. This is an open access article under the CC BY-NC-ND license (<http://creativecommons.org/licenses/by-nc-nd/4.0/>).

provide inspiration for designing scaffolds for bone regeneration. Playing a role like stairs, the consecutive and gentle slope of the spiral structure in the conches can predictably reduce the difficulty of movement for the anti-gravity direction. Consequently, integrating the conch-like (CL) structure into the 3D-printed scaffolds is a promising approach to achieve directionally guided bone growth by promoting the migration and penetration of cells, tissues and nutrients in a specific direction.

In terms of composition, the main component of natural conch shells is  $\text{CaCO}_3$  (aragonite) with a content of about 95%, which is a common bioceramic material [35]. Bioceramics, as a kind of typical biomaterials, have been widely studied in tissue engineering, because of their excellent mechanical properties, good biocompatibility and osteogenic activity [36–38]. Since the 20th century, bioceramics have gained rapid development from the original bioinert ceramic materials such as alumina ( $\text{Al}_2\text{O}_3$ ) and zirconia ( $\text{Zr}_2\text{O}_3$ ) to the current bioactive ceramics with tissue induction and regeneration functions [39,40]. So far, scaffolds based on different bioceramic materials have also been widely used in bone tissue engineering [14,41].  $\beta$ -TCP, as a representative of calcium phosphate bioceramics, has been widely used in clinical repair of bone defects owing to the excellent biocompatibility, degradability, osteoconductivity and similarity to the inorganic component of human bone [36,38,42,43]. Therefore, in this work,  $\beta$ -TCP bioceramic was selected to prepare 3D-printed scaffolds to simulate  $\text{CaCO}_3$  in natural conch shells.

Herein, inspired by the unique structure and growth process of conches, based on  $\beta$ -TCP bioceramic material, a “cells climbing stairs”-like scaffolds for guiding directional bone growth were successfully prepared via 3D printing technology with digital light processing (DLP) (Fig. 1). The biomimetic scaffolds with CL structure were composed of spiral sections and cavities, as well as intermediate support spar and peripheral wall containing through macropores, which could be well regulated with accuracy and flexibility by the 3D printing technology. The CL scaffolds could guide and promote tissue cells to migrate along vertical direction. The spiral sections in the scaffolds could act as “stairs” to direct the cells climbing from the bottom to the top of the scaffolds. Meanwhile, compared with the conventional cross-strut (Cross) scaffolds, the CL scaffolds exhibited improved mechanical properties, better material transport performance and stimulatory effect on the cell adhesion, proliferation as well as subsequent osteogenic differentiation *in vitro*. Furthermore, we verified that the CL scaffolds could well guide the directional growth of bone tissue from the bottom to the top of scaffolds with a special half-embedded femoral defects model *in vivo*.

The new bone tissue obviously grew to the protruded part of the scaffolds along the spiral structure. Therefore, it is believed that the prepared CL bioceramic scaffolds will be a promising candidate for guiding directional bone growth to repair severe bone defects.

## 2. Materials and methods

### 2.1. Materials

Conches were purchased from Alibaba Group (China). All reagents were used as received without further processed.

**Preparation of the precursor slurry:** The precursor slurry with a theoretical solid content of 55 wt% was prepared by the following method. 80 g of bioceramic powder  $\beta$ -TCP ( $\beta$ - $\text{Ca}_3(\text{PO}_4)_2$ , HQ-TCP-01, Kunshan Chinese Technology New Materials Co., Ltd., China), 35 g photosensitive resin (Wanhao Factory Co., Ltd., China), 20 g HDDA (1,6-hexanediol diacrylate, 90%, Shanghai Macklin Biochemical Co., Ltd., China), 6 g Triton X-100 (AR, Shanghai Macklin Biochemical Co., Ltd., China), 4 g KH570 (98.0%, Sinopharm Chemical Reagent Co., Ltd., China), and 0.5 g DPO (diphenyl (2,4,6-trimethylbenzoyl) phosphine oxide, 97%, Aladdin, China) were ball-milling mixed by planetary ball mill (QM-3SP2, Nanjing University Instrument Factory, China) at a speed of  $500 \text{ min}^{-1}$  for 8 h.

### 2.2. Fabrication of the CL scaffolds

The overall fabrication process was shown in Fig. S2A. Specifically, the 3D models with varied structural parameters of CL scaffolds were designed with SolidWorks software (SolidWorks 2016, Dassault systems, France) and converted into stereolithography (STL) file format. Then, the precursor slurry was added to the DLP-based light curing 3D printer (AUTOCERA-M, Beijing TenDimensions Technology Co., Ltd., China) and printed layer by layer according to the STL file. The printed layer thickness was fixed at  $50 \mu\text{m}$ . In addition, the wavelength of the curing light source was 405 nm. The exposure time of the first layer was 40 s and the others were 8 s. After printed, the samples were removed from the printing platform and ultrasonically cleaned with alcohol for 20 s carefully. The cleaning step was repeated twice to remove the residual slurry. Then, the cleaned green bodies were placed under a 405 nm portable light source for 1 h for secondary curing. Finally, the green bodies were debinded and sintered in muffle furnace (SSJ-14, Luoyang Shenjia, Kiln. Co., Ltd., China). The sintering procedure was as follows:

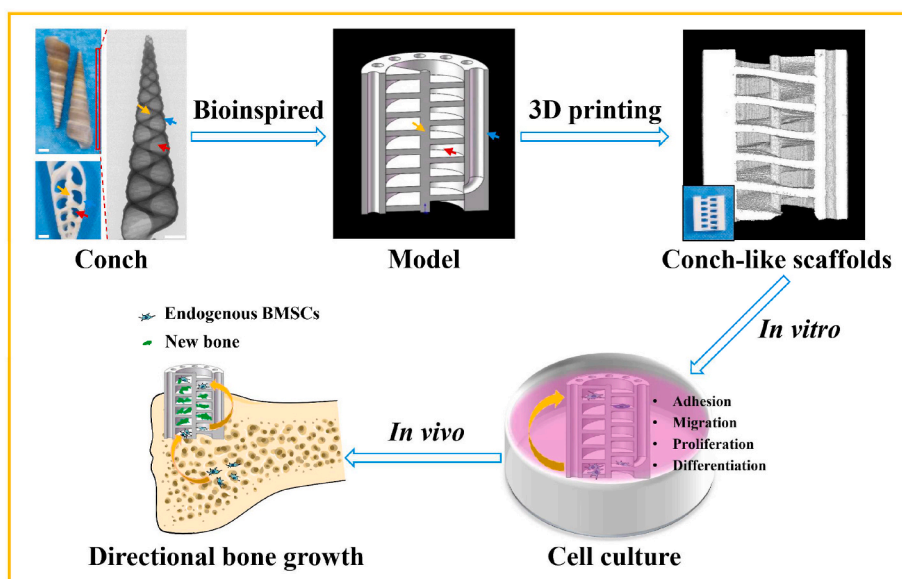


**Fig. 1.** Schematic illustration of the preparation and application in guiding directional bone growth of the 3D-printed CL scaffolds inspired by the features of natural conches. The biomimetic scaffolds were comprised of spiral sections and cavities, as well as intermediate support spar and peripheral wall with through macropores. Benefiting from the spiral biomimetic structure, the CL scaffolds greatly enhanced cell behaviors including adhesion, proliferation, osteogenic differentiation, and significantly promoted cell migration from the bottom to the top of the scaffolds, which was like “cells climbing stairs”. Furthermore, the CL scaffolds well guided the bottom-up directional bone growth *in vivo*, similar to the growth process of natural conches.

firstly, it increased from room temperature to 300 °C at the rate of 1 °C min<sup>-1</sup> and maintained for 2 h; then, the temperature rose to 650 °C at the rate of 0.5 °C min<sup>-1</sup> and kept for 2 h; finally, the temperature rose to 1150 °C at the rate of 2 °C min<sup>-1</sup> and kept for 3 h.

### 2.3. Characterization of the CL scaffolds

The synchronous thermal analyzer (STA, STA 449C, Netzsch, Germany) was used to test the weight and heat changes of the 3D-printed green bodies from room temperature to 1200 °C in air atmosphere at a heating rate of 10 °C min<sup>-1</sup>. XRD (D8 ADVANCE, Bruker, Germany) was conducted to characterize the phase composition of the  $\beta$ -TCP powders and sintered ceramic scaffolds. The dimensions of the scaffolds after printed and sintered were measured with vernier caliper (Nanjing Suce Measuring Instrument Co., Ltd., China). Six replicates were used in each group. The photographs of the scaffolds and natural conches were taken by a digital camera (D90, Nikon, Japan). The 3D images of the ceramic scaffolds ( $\Phi = 9.8$  mm, H = 11.0 mm) and natural conches were reconstructed by Micro-CT (SKYSCAN1172, Bruker, Germany), which was also used to analyze the porosity of ceramic scaffolds. Three replicates were prepared for each group. The morphology and structure of the scaffolds were further observed by SEM (S-4800, Hitachi, Japan).

**Mechanical tests of the CL scaffolds:** The mechanical properties were all measured by universal testing machine of mechanics of materials (INSTRON-5566, Instron, USA) in room temperature. Specifically, for compressive properties, the ceramic scaffolds samples were fabricated with size  $\Phi = 9.8$  mm and H = 11.0 mm (model:  $\Phi = 13.0$  mm, H = 15.0 mm). And the loading rate of the test was 0.5 mm min<sup>-1</sup>. Compressive strength and modulus were respectively defined as the maximum value of the compressive stress-strain curve and the slope of the linear stage of the initial stress-strain curve. For flexural properties, the ceramic samples for three-point bending test were prepared with size  $\Phi = 9.8$  mm and H = 22.0 mm (model:  $\Phi = 13.0$  mm, H = 30.0 mm). The test span was 18.0 mm with loading rate of 0.5 mm min<sup>-1</sup>. The flexural strength and modulus were defined as the maximum value of the flexural stress-strain curve and the slope of the linear stage of the initial stress-strain curve, respectively. Six replicates were used in each group.

**Material transport tests of the CL scaffolds:** The liquid transport experiment was performed to evaluate the material transport properties of the CL scaffolds. Briefly, the ceramic scaffolds samples with a partly bottom-up opening on the side were fabricated with size  $\Phi = 9.8$  mm and H = 7.5 mm (model:  $\Phi = 13.0$  mm, H = 10.0 mm). Then, the bottom of different scaffolds were immersed in simulate body fluid (SBF) solution labeled with red ink (The height of SBF solution at the place where the scaffolds was placed was 1.5 mm). The liquid transport process of scaffolds was recorded with a digital camera (D90, Nikon, Japan). All movies were slow played at 8x speed by PotPlayer software (Daum, Korea) and exported as pictures at corresponding time points frame by frame. The highest height of labeled SBF solution in different scaffolds at certain time points were measured by ImageJ software (National Institutes of Health, USA). Three replicates were prepared for each group.

### 2.4. Bioactivity experiments in vitro

The rabbit bone marrow stem cells (rBMSCs) were extracted from the hind leg femurs of 4-week-old New Zealand white rabbits (Shanghai Jiagan Biotechnology Co., Ltd., China) and cultured in the low glucose-type Dulbecco's modified Eagle medium (DMEM, SANGON Biotech Co., Ltd., China) supplemented with 10% fetal bovine serum (FBS, HyClone Co., Ltd., China), 1% penicillin/streptomycin (P/S, HyClone Co., Ltd., China) and 1% glutamine (Gln, SANGON Biotech Co., Ltd., China). All scaffolds used in the follow-up studies were sterilized by autoclaving.

**Cell distribution experiment:** For the evaluation of cell distribution in the scaffolds, the bottom-sealed CL scaffolds with P = 1.6 mm were put within a 48-well plate. 150  $\mu$ L rBMSCs suspension was seeded in each scaffold (150  $\mu$ L, and the concentration of cell suspension was  $2 \times 10^5$

cells mL<sup>-1</sup>, so  $3 \times 10^4$  cells scaffold<sup>-1</sup> in total). After seeding cells, 200  $\mu$ L culture medium was carefully added around the scaffolds to keep wet. Then the scaffolds were incubated at 37 °C in a 5% CO<sub>2</sub> cell incubator (ThermoFisher, USA) for 4 h to make cells adhered. Subsequently, culture medium was blotted up by vacuum pump, and 800  $\mu$ L culture medium was added to the each well to completely submerge the scaffolds. One day later, the cells were fixed with 4% paraformaldehyde fix solution (SANGON Biotech Co., Ltd., China) for 30 min and permeated with 0.1% Triton X-100 for 5 min. Next, the cytoskeleton was stained with fluorescein isothiocyanate phalloidin (FITC, green, Sigma-Aldrich, USA) for 45 min. After brief washing with PBS, the nuclei were stained with 4',6-diamidino-2-phenylindole (DAPI, blue, Sigma-Aldrich, USA) for 7 min. And PBS was used to briefly rinse the scaffolds again. Finally, the images of cells in the scaffolds were captured by confocal laser scanning microscope (CLSM, TCS SP8, Leica, Germany), which reflected the cell distribution and morphology in different parts (i.e., different layers) of the scaffolds. Whenever the cells in the top layer were photographed, this layer would be carefully stripped and removed with tweezers to expose the next hidden lower layer of the scaffolds. The above operations were repeated to observe the cells on the 1st, 2nd, 3rd and 4th layers of the scaffolds in order to analyze the cell distribution in different parts.

**Cell adhesion and delivery assay:** For the evaluation of cell adhesion and delivery of the CL scaffolds, the scaffolds with unsealed bottom were employ for the assay. Four experimental groups were investigated (Cross, P = 1.6, 2.0 and 2.4). Scaffolds were placed in 48 well-plates. And 800  $\mu$ L rBMSCs suspension was seeded into each well (800  $\mu$ L, and  $6.75 \times 10^5$  cells mL<sup>-1</sup>, so  $5.4 \times 10^4$  cells well<sup>-1</sup> in total), so that the cell suspension could completely immerse the scaffolds and evenly distribute in the wells. The cells seeded on the plates were considered as the positive control and the empty wells were considered as the negative control. After incubated for 4, 12 and 24 h respectively, the cell-loading scaffolds were carefully washed twice with PBS to remove nonadherent cells and then transferred to new wells. At each time point, 800  $\mu$ L of culture medium with 10% CCK-8 (cell counting kit-8, Beyotime, China) was added to the wells for 4.5 h. Subsequently, the absorbance was measured at  $\lambda = 450$  nm in a multifunction microplate reader (SpectraFluor Plus, Tecan, Germany) to quantify the cells loading in the scaffolds. Six replicates were prepared for each group. In likewise, 800, 400 and 200  $\mu$ L of the previous cell suspension were respectively added to the wells without any scaffold. Then, 0, 400 and 600  $\mu$ L of culture medium were added to these wells, respectively. After incubated for 4 h, they were used as positive controls for complete attachment. And the growth medium was replaced by culture medium with CCK-8 for 4.5 h. The absorbance value at 450 nm was measured as the standard curve reflecting the relationship between cells number and absorbance value. Three replicates were prepared for each group. All the results were presented as optical density (OD) values minus the absorbance of blank wells. In addition, the scaffolds were fixed with 4% paraformaldehyde fix solution for 30 min after cultured for 24 h. Then the cytoskeleton and nuclei of the cells were stained with FITC (green) and DAPI (blue), respectively. The distribution and morphology of cells in the upper layer of varied scaffolds were characterized by CLSM. And the orientation angle of rBMSCs adhered on the scaffolds in CLSM images was measured by Photoshop software (CS6, Adobe, USA). Twenty cells were measured in each group.

**Cell viability assay:** The live/dead staining assay was performed to evaluate the viability of rBMSCs in the scaffolds, and the scaffolds with sealed bottom were applied for this assay. Five experimental groups were investigated (Blank, Cross, P = 1.6, 2.0 and 2.4). The bottom-sealed scaffolds were placed in 24 well-plates. 80  $\mu$ L of rBMSCs suspension was seeded into each well (80  $\mu$ L, and  $1.25 \times 10^5$  cells mL<sup>-1</sup>, so  $1 \times 10^4$  cells scaffold<sup>-1</sup> in total), and 200  $\mu$ L culture medium was carefully added around the scaffolds to keep wet. The scaffolds were incubated for 4 h to make the cells adhered. After that, 800  $\mu$ L culture medium was added in each well to completely submerge the scaffolds.

And the seeded rBMSCs were cultured for 2 days. Subsequently, the Calcein-AM/PI double staining kit (Dojindo, Japan) was diluted with PBS in a volume ratio of PBS: AM: PI = 1000: 2: 3. The scaffolds and blank wells were washed with PBS for 2 times and then added with the live/dead staining working solution. After incubated at 37 °C for 25 min, the scaffolds and blank wells were observed by CLSM (FV1000, Olympus, Japan). Live cells were stained in green with 488 nm excitation lights while dead cells were stained in red with 559 nm excitation lights.

**Cell proliferation assay:** For the evaluation of cell proliferation of the CL scaffolds, the scaffolds with sealed bottom were applied for the assay. Four experimental groups were investigated (Cross, P = 1.6, 2.0 and 2.4). The bottom-sealed scaffolds were placed in 48 well-plates. 80  $\mu\text{L}$  of rBMSCs suspension was seeded into each well with scaffold (80  $\mu\text{L}$ , and  $1.25 \times 10^5$  cells  $\text{mL}^{-1}$ , so  $1 \times 10^4$  cells scaffold $^{-1}$  in total), and 100  $\mu\text{L}$  culture medium was carefully added around the scaffolds to keep wet. Then the scaffolds were incubated for 4 h to make the cells adhered. After that, 400  $\mu\text{L}$  culture medium was added in each well to completely submerge the scaffolds. The medium was changed every 2 days. At each time point (1, 3 and 7 days), the medium was replaced by culture medium with 10% CCK-8 for 4.5 h. The absorbance was measured at  $\lambda = 450$  nm in a multifunction microplate reader. Three replicates were prepared for each group.

**Cell migration assay:** For the evaluation of cell migration of the CL scaffolds, four experimental groups were investigated (Cross, P = 1.6, 2.0 and 2.4). The rBMSCs were cultured in the medium (the low glucose-type DMEM supplemented with 5% FBS respectively). The bottom-sealed scaffolds were placed in 24 well-plates. Through the cell-seeding channel of scaffolds, 40  $\mu\text{L}$  of cell suspension was carefully added to the lower 1–2 layers of each scaffold from bottom to top (40  $\mu\text{L}$ , and  $1.0 \times 10^6$  cells  $\text{mL}^{-1}$ , so  $4 \times 10^4$  cells scaffold $^{-1}$  in total). Then, 200  $\mu\text{L}$  medium was added around the scaffolds to keep wet. After incubated for 4 h, the cell-loading scaffolds were carefully washed twice with PBS to remove nonadherent cells. Then another 1 mL medium was added in each well to completely submerge the scaffolds. The medium was changed every 2 days. Samples were taken after 1 and 10 days respectively to determine the initial position of cells added and the final position after migrating. In order to observe the distribution of cells in scaffolds, the scaffolds were fixed with 4% paraformaldehyde fix solution. Subsequently, the cytoskeleton and nuclei were stained with FITC and DAPI, respectively. And the scaffolds were imaged with CLSM to characterize the initial position of cell distribution at 1 day and the final position of cell distribution after migrating for 10 days. The migration capabilities in Z direction (vertical direction) and XY direction (horizontal direction) were respectively quantified by the number change of printing steps and the angle change of relative center rotation between the initial position and final position of cells distribution in CLSM images. Five replicates were used in each group. And the orientation angle of rBMSCs after migrating for 10 days in CLSM images was measured by Photoshop software. Twenty cells were measured in each group.

**Gene and protein expression of cells:** To explore the gene expression of the cells in CL scaffolds, the bottom-sealed scaffolds were applied in the assay. Four groups of the scaffolds (Cross, P = 1.6, 2.0 and 2.4) were investigated. The rBMSCs were cultured in differentiation medium (DMEM complete medium supplemented with  $1.0 \times 10^{-2}$  M  $\beta$ -glycerol phosphate and  $2.0 \times 10^{-4}$  M ascorbic acid). Firstly, the scaffolds were placed in 24 well-plates. Through the cell-seeding channel, 100  $\mu\text{L}$  cell suspension was carefully added to each scaffold (100  $\mu\text{L}$ , and  $5 \times 10^5$  cells  $\text{mL}^{-1}$ , so  $5 \times 10^4$  cells scaffold $^{-1}$ ). Then, 200  $\mu\text{L}$  of culture medium was added around the scaffolds to keep wet. For the blank wells without any scaffolds, 100  $\mu\text{L}$  cell suspension and 200  $\mu\text{L}$  culture medium were added too. After incubated for 4 h, culture medium was blotted up by vacuum pump. The scaffolds were then incubated at 37 °C for 4 h to allow the cells adhered. After that, another 700  $\mu\text{L}$  medium was added to each well to completely submerge the scaffolds. The medium was changed every 2 days. After incubated for 7 days, the total RNA was

extracted by Trizol Reagent (Invitrogen Trizol, ThermoFisher, USA). Complementary DNA (cDNA) was prepared by PrimeScript 1st Strand cDNA synthesis Kit (TOYOBO, Japan). GAPDH was as the endogenous control, and quantitative reverse transcription PCR (RT-qPCR) was performed with SYBR Green qPCR Master Mix (Takara, Japan). The expression of relative osteogenic genes: BSP, OCN, OPN, BMP2 and Runx2 were calculated by the  $2^{-\Delta\Delta\text{Ct}}$  method. Four replicates were used in each group. The primer sequences were shown in Table S2. Furthermore, for the characterization of osteogenic relative proteins, two groups of the scaffolds (Cross and P = 2.4) were selected. In short, the scaffolds were treated with the corresponding primary antibody of bone sialoprotein (BSP, sc-292393, Santa Cruz Biotechnology, Inc., USA) and osteocalcin (OCN, sc-30044, Santa Cruz Biotechnology, Inc., USA) and fluorescent secondary antibody (red, A-21245, ThermoFisher, USA). Then the cytoskeleton and nuclei were stained with FITC (green) and DAPI (blue), respectively. Subsequently, CLSM was used to characterize the expression of specific osteogenic relative proteins in scaffolds at 7 days. And the semi-quantitative analyses were processed by Image J software. Three replicates were prepared for each group.

**Alizarin red S (ARS) staining assay:** ARS staining was used to evaluate the osteogenic differentiation of rBMSCs in the CL scaffolds *in vitro*. For the evaluation of ARS staining of the CL scaffolds, the scaffolds with sealed bottom were applied for the assay. Four experimental groups were investigated (Cross, P = 1.6, 2.0 and 2.4). And the scaffolds without rBMSCs seeded were used as negative control. The bottom-sealed scaffolds were placed in 24 well-plates. 100  $\mu\text{L}$  of rBMSCs suspension was seeded into each well with scaffold (100  $\mu\text{L}$ , and  $2 \times 10^5$  cells  $\text{mL}^{-1}$ , so  $2 \times 10^4$  cells scaffold $^{-1}$  in total), and 200  $\mu\text{L}$  culture medium was carefully added around the scaffolds to keep wet. Then the scaffolds were incubated for 4 h to make the cells adhered. After that, another 700  $\mu\text{L}$  culture medium was added in each well to completely submerge the scaffolds. The medium was changed every 2 days. After cultured for 7 days, the scaffolds were washed with PBS and fixed in 4% paraformaldehyde for 30 min, then stained with ARS solution (0.2%, pH = 8.3, Beyotime, China) for 30 min at 37 °C. After that, the scaffolds were washed with PBS to remove the residue ARS solution and imaged by a digital camera. In order to quantification of the alizarin red S staining value, the scaffolds were incubated with 10% acetic acid (AR, Sinopharm Chemical Reagent Co., Ltd., China) overnight and neutralized with 10% ammonia solution (25%–28%, Shanghai LINGFENG Chemical Reagent Co., Ltd., China). Then the absorbance of supernatant was measured at  $\lambda = 450$  nm in a multifunction microplate reader. Three replicates were prepared for each group.

**Ionic release of the CL scaffolds:** In order to evaluate the Ca and P ions released from the scaffolds, the 3D CL scaffolds were cultured in 1 mL low glucose-type DMEM at cell incubator with 5%  $\text{CO}_2$  at 37 °C. The medium was collected and filtered at 1, 3, 5 and 7 days. And the medium was renewed at each time point. The concentration of Ca and P ions in the medium were tested by the inductively coupled plasma atomic emission spectroscopy (ICP-AES, Varian 715 ES, Palo Alto, USA). Three replicates were prepared for each group.

## 2.5. Bioactivity experiments *in vivo*

**Bone defect regeneration:** All the animal experiments were approved by the Institutional Animal Care and Use Committee of Nanjing First Hospital, Nanjing Medical University and carried out in strict accordance with relevant laws and guidelines. The scaffolds with size of  $\Phi = 6.0$  mm and H = 7.5 mm were used to evaluate the osteogenesis processes *in vivo*. A total of 18 male New Zealand white rabbits (2.5–3 kg) were selected for the experiments and randomly divided into three groups: Blank, Cross and P = 2.4. The femoral defect with a diameter of 6.0 mm and a depth of about 5.0 mm was constructed with a hand-held electric-drill (RA-II, YANCHENG RUIAO KEJI Co., Ltd., China). Then, two kinds of scaffolds (Cross and P = 2.4) were implanted into the defects, respectively. It was ensured that the scaffolds were embedded for

~5 mm and protruded about ~2.5 mm, which was called half-embedded bone defects model (HE-BDM). After 8 and 12 weeks of implantation, rabbits were sacrificed respectively. The femoral samples were collected from the rabbits and fixed with 4% paraformaldehyde fix solution (SANGON Biotech. Co., Ltd., China) for 48 h.

**Micro-CT analysis:** To investigate the effect on new bone formation *in vivo*, Micro-CT (SKYSCAN 1172, Bruker, Germany) was used to scan the samples with a resolution of 8.9  $\mu\text{m}$ . The respective threshold ranges of rabbit bone and scaffolds in Micro-CT analysis were 50–130 and 130–255 respectively. The new bone regeneration was estimated by the newly formed bone volume to the total volume (BV/TV) ratio and the new trabecular number (Tb. N) for varied parts. In addition, the scaffolds were reconstructed to determine the effect of bone regeneration in different parts (scaffolds: red; newly formed bone: green). Four replicates were used in each group.

**Histological staining analysis:** The harvested samples were gradient dehydrated with 70, 80, 90, 95, 100, 100% (v/v) alcohol aqueous solution. After that, the samples were embedded in poly-methyl methacrylate (PMMA, Aladdin, China), and sectioned at 600  $\mu\text{m}$  by a microtome (SP1600, Leica, Germany). After polished by a polishing machine (LaboPol-5, Struers, Denmark), the sections were stained with Van Gieson's picrofuchsin (VG) dye to evaluate the newly formed bone tissue (scaffolds: black; new bone: red).

## 2.6. Statistical analysis

All data were presented as the mean  $\pm$  standard deviation (SD). The number of statistical samples in each group shouldn't be less than three. The post-hoc test was chosen for one-way ANOVA. The statistical analysis was performed using Tukey test in Origin 2018 software (OriginLab, USA). A *P*-value less than 0.05 was considered as significant difference. Concretely, <sup>ns</sup>*P*  $\geq$  0.05, \**P* < 0.05, \*\**P* < 0.01, \*\*\**P* < 0.001.

## 3. Results and discussion

### 3.1. Fabrication and characterization of the CL scaffolds

$\beta$ -TCP, a representative bioactive ceramic material, was widely used in bone tissue engineering research and clinical application for its excellent bioactivity, appropriate degradation rate, osteoconductivity and similarity to the inorganic component of human bone [36,44,45]. Therefore,  $\beta$ -TCP bioceramic was selected as the basic material to fabricate the scaffolds in this study to replace  $\text{CaCO}_3$  in natural conch shells. Referring to the features of natural conches, the CL bioceramic scaffolds were successfully fabricated *via* DLP-based 3D printing technology. As shown in Fig. 1, the CL scaffolds were composed of spiral sections and cavities, as well as intermediate support spar and peripheral wall containing through macropores. Notably, the vertical distance between a point on one spiral layer and the corresponding point on the adjacent spiral layer in the spiral structure of the CL scaffolds was defined as the pitch of screw (*P*). And the *P* could be well modulated with 1.6, 2.0 and 2.4 mm (Figs. S1B–D and Fig. 2B–D). The intermediate support spar and peripheral wall were designed to endow the scaffolds with good structural support and stability. Besides, in order to adjust the porosity and mechanical properties of scaffolds, upright through macropores (Fig. 2E) were added in the peripheral wall, and one of macropores was replaced by the channel with a diameter of 1.5 mm (Fig. 2F) for subsequent cell seeding. As known, conventional 3D-printed scaffolds were usually composed of solid struts stacked in cross. Thus, the cross-strut (Cross) scaffolds (Fig. S1A and Fig. 2A), with solid struts stacked in cross at 45°, were used as the control group. Notably, all groups of scaffolds were designed with approximate porosity (Table S1). It is worth mentioning that the bottom of the scaffolds was open for testing porosity, mechanical properties, material transport properties, cell adhesion and *in vivo* experiments, while it was sealed for testing cell uniformity, live/dead staining, cell proliferation, cell migration, cell

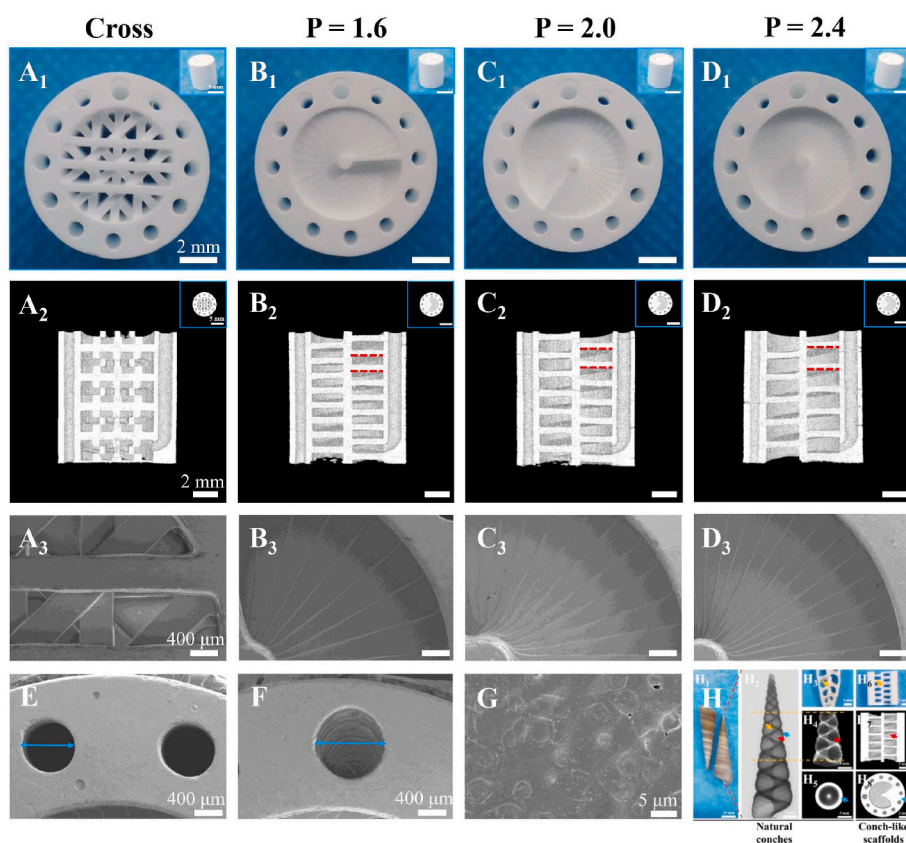


**Fig. 2.** Structure and morphology characterization of the 3D-printed CL scaffolds and the natural conches. Digital photograph of the conventional cross-strut scaffolds (A<sub>1</sub>) and the CL scaffolds with varied pitches (B<sub>1</sub>–D<sub>1</sub>) (*P* = 1.6, 2.0 and 2.4 mm, *D* = 1.2 mm, *N* = 12) in vertical view (the inset figures showed the side-view digital photograph of corresponding scaffolds, scale bars = 5 mm), scale bars = 2 mm. (A<sub>2</sub>–D<sub>2</sub>) The sagittal Micro-CT reconstruction images of the scaffolds to show their spiral structure in the inner of CL scaffolds (the inset figures showed the transverse view, scale bars = 5 mm), scale bars = 2 mm. (A<sub>3</sub>–D<sub>3</sub>) The representative SEM images of scaffolds, scale bars = 400  $\mu\text{m}$ . (E) SEM image for through macropores in the peripheral wall ( $\phi$  = 1.2 mm in model), scale bar = 400  $\mu\text{m}$ . (F) SEM image for cell-seeding channel in the peripheral wall ( $\phi$  = 1.5 mm in model), scale bar = 400  $\mu\text{m}$ . (G) SEM image for the surface of scaffolds, scale bar = 5  $\mu\text{m}$ . (H) Structure and morphology characterization of natural conches, and the similarity in structure between the natural conches and 3D-printed CL scaffolds (*P* = 2.4 mm, *N* = 12, *D* = 1.2 mm). Specifically, digital photograph (H<sub>1</sub>) and Micro-CT image (H<sub>2</sub>) of the natural conches (*turritella terebra*), scale bars = 10, 5 mm. Digital photograph of the double sagittal section of the natural conches (*terebra maculata*), scale bar = 5 mm (H<sub>3</sub>). Sagittal section (H<sub>4</sub>) and transverse section (H<sub>5</sub>) images of the natural conches (*turritella terebra*) in H<sub>2</sub>, scale bars = 5 mm. Digital photograph of the double sagittal section of the 3D-printed CL scaffolds, scale bar = 2 mm (H<sub>6</sub>). Sagittal section (H<sub>7</sub>) and transverse section (H<sub>8</sub>) images of the 3D-printed CL scaffolds (*P* = 2.4 mm), scale bars = 2 mm.

osteogenic differentiation, alizarin red S staining and ionic release to well load the seeded cells.

The morphology, composition and structure of the 3D-printed bioceramic scaffolds were characterized. Firstly, the scaffolds were highly consistent with the models (Fig. S1 and Fig. 2A<sub>2</sub>-D<sub>2</sub>). No obvious defects, such as deformations and cracks were observed in the scaffolds (Fig. 2A–G). Besides, the surface micromorphology of the sintered scaffolds was dense as shown in Fig. 2G. Notably, due to the layer-by-layer curing mode of DLP-based 3D printing, the spiral structure with stepped characteristic was produced in the varied CL scaffolds, which was like stairs (Fig. 2B<sub>3</sub>-D<sub>3</sub>). Furthermore, the fabricated CL scaffolds showed quite similar structure with the natural conches (Fig. 2H). Then, the curves of thermal analysis showed that the ceramic particles content of green body was 57.1 wt% (Fig. S2B), which was slightly higher than the theoretical value, which might be due to the loss of resin in the process of adding ceramic powder several times. XRD analysis indicated that the sintered scaffolds possess the pure crystal phase of  $\beta$ -TCP (PDF# 09-0169) (Fig. S2C). By measuring the dimensions of the green bodies and sintered scaffolds, it was found that the DLP-based 3D printing revealed a high precision (more than 95%) in either XY or Z direction (Fig. S2D). And the shrinkage rate of the sintered scaffolds was uniform in all directions for about 24% (Fig. S2E). Thus, the size and structure of the CL bioceramic scaffolds could be well controlled by the DLP-based 3D printing processes.

In order to explore the relationship among structural parameters, porosity and mechanical properties, scaffolds with a diameter of 13.0 mm and height of 15.0/30.0 mm were designed with varied pitches of screw (movie S1 and S4), numbers (N) of macropores (movie S2 and S5), and diameters (D) of macropores (movie S3 and S6). With the increase of pitches, the porosity (Fig. 3A) of scaffolds increased, while the compressive strength (Fig. 3B) and compressive modulus (Fig. 3C) first decreased and then slightly increased. As for the flexural strength (Fig. 3F) and flexural modulus (Fig. 3G) of scaffolds, they gradually decreased. Notably, the compressive strength, compressive modulus, flexural strength and flexural modulus of the CL scaffolds ( $P = 2.0$  mm) showed remarkable increase of 65.3%, 30.2%, 100.7% and 39.5%, respectively, as compared to those of the Cross scaffolds with similar porosity (37%). The results indicated that mechanical properties of the CL scaffolds were significantly improved as compared with the conventional Cross scaffolds. It could be explained by the natural spiral structure of conches was more effective in protecting the outer surface from high stress than the simpler shape [34].

Supplementary data related to this article can be found at <https://doi.org/10.1016/j.bioactmat.2022.09.014>.

However, it might be difficult to satisfy the diversified clinical needs for the porosity and mechanical properties of the of bioceramic scaffolds by merely changing pitches. Moreover, the CL scaffolds with varied numbers and diameters of macropores were prepared to further explore their physical properties. For the CL scaffolds with  $P = 2.4$  mm, the numbers of macropores could be changed to 8, 12 and 16 (Figs. S3A–C). It was found that, with the numbers of macropores increasing, the porosity (Fig. S3D) of scaffolds increased, while the compressive strength (Figs. S3E and G) and compressive modulus (Figs. S3F and G) firstly increased and then decreased. Meantime, both the flexural strength (Figs. S3H and I) and flexural modulus (Figs. S3H and J) gradually decreased with number of macropores increasing. Therefore, the scaffolds with  $N = 12$  possessed the highest compressive strength. Besides, for the CL scaffolds with  $P = 2.4$  mm and  $N = 12$ , the diameters of through macropores could be designed as 1.0, 1.2 and 1.5 mm (Figs. S4A–C). As the diameters of macropores increased, the porosity (Fig. S4D) of scaffolds increased, while compressive strength (Figs. S4E and G) and compressive modulus (Figs. S4E and H) gradually decreased. Meanwhile, both the flexural strength (Figs. S4F and I) and flexural modulus (Figs. S4F and J) showed a trend of first decrease and then increase. Considering the porosity and mechanical properties comprehensively, the scaffold with  $N = 12$  and  $D = 1.2$  mm was chosen as a representative for the subsequent experiments.

Consequently, the porosity and mechanical properties of the CL scaffolds could be well controlled by varying the structural parameters, which was of great importance to satisfy different mechanical requirements in clinic. More specifically, the CL scaffolds revealed a range of 33.4–43.8% for porosity, 11.2–38.7 MPa for compressive strength, 0.63–1.73 GPa for compressive modulus, 2.71–9.95 MPa for flexural strength and 0.74–1.19 GPa for flexural modulus. Therefore, it was suggested that the 3D-printed CL scaffolds with tunable structural and physical properties were successfully fabricated.

The material transport properties of the CL scaffolds were further characterized, which may have an effect on cell behaviors and bone regeneration. The liquid transport experiment was performed to evaluate the material transport properties of the CL scaffolds. The scaffolds with a partly bottom-up opening on the side were prepared for this experiment (movie S7). And the bottom of the scaffolds were immersed in SBF labeled with red ink and the liquid transport process was recorded. As shown in Fig. S5. The results showed that the red SBF solution

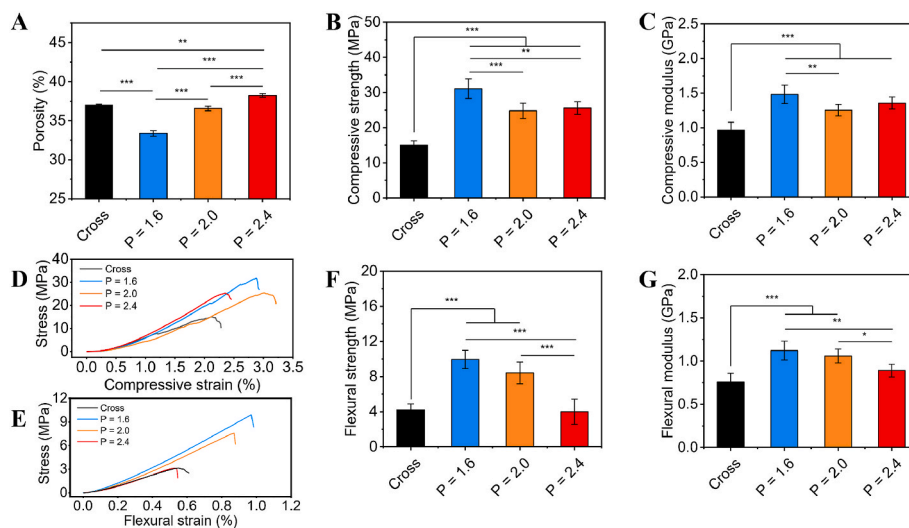


**Fig. 3.** Porosity and mechanical properties of the 3D-printed CL scaffolds ( $N = 12$ ,  $D = 1.2$  mm) with varied pitches. (A) Porosity of the 3D-printed scaffolds. Compressive strength (B) and compressive modulus (C) of the 3D-printed scaffolds. Typical compressive stress-strain curves (D) and flexural stress-strain curves (E) of the 3D-printed scaffolds. Flexural strength (F) and flexural modulus (G) of the 3D-printed scaffolds. ( $n = 6$ ,  $*P < 0.05$ ,  $**P < 0.01$ ,  $***P < 0.001$ ).

increased rapidly within 0.8 s and reached the top of all scaffolds with the same height ( $H = 7.5$  mm) (Figs. S5A–B). However, it could be found that the rising speed of liquid level and the total time for varied scaffolds were different (Figs. S5B–C). The slight difference in the highest height of liquid level was probably due to the slight difference in the absorbed liquid volume caused by the porosity difference of the varied scaffolds. The  $P = 1.6$  group had the similar rising speed of liquid level and total time as the Cross group, while the  $P = 2.0$  group had significantly faster rising speed and shorter total time compared with the Cross group. Moreover, the  $P = 2.4$  group had significantly the fastest rising speed of liquid level and the shortest total time as compared to the Cross group and  $P = 1.6$  group. This indicated that with the increase of pitches, the liquid transport capacity of the CL scaffold was gradually improved. On the one hand, with the pitches increasing, the porosity increased, and the transportation path of the liquid in the spiral structure for the CL scaffolds was gradually shortened (movie S8–S11). On the other hand, it might be caused by the difference in the additional pressure generated by the curved liquid surface of the spiral structure surface infiltrated by capillary action. The varied curvature of the spiral structure with stepped characteristic of the CL scaffolds, might lead to different driving forces for the rising of liquid level. Capillarity is the primary force for many plants to absorb and transport nutrients from the soil [46]. Therefore, the improved liquid transport ability of the CL scaffolds implied that the CL scaffolds had better material transport performance with the increase of pitches. This may have a positive impact on the transport of nutrients and oxygen during *in vitro* cell culture and *in vivo* bone regeneration.

Supplementary data related to this article can be found at <https://doi.org/10.1016/j.bioactmat.2022.09.014>.

### 3.2. Cell adhesion, viability and proliferation assays *in vitro*

In order to investigate whether the spiral structure of CL scaffolds influence cell behaviors, the CL scaffolds with varied pitches ( $P = 1.6$ , 2.0 and 2.4 mm) were prepared, and the conventional Cross scaffolds were set as the control group. Rabbit bone marrow mesenchymal stem cells (rBMSCs) were seeded in the scaffolds to study the effects of CL scaffolds on cell behaviors *in vitro*.

The adhesion, viability and proliferation activities of the cells seeded in 3D-printed CL scaffolds were firstly investigated. The CL scaffolds with  $P = 1.6$  mm were selected for the test of cell distribution uniformity (movie S12). The distribution and morphology of rBMSCs seeded on different layers of the CL scaffolds were observed by confocal laser scanning microscope (CLSM). As shown in Fig. S6, the seeded rBMSCs were uniformly distributed in each layer of the scaffolds after cultured for 1 day. In addition, the rBMSCs were well spread with aligned arrangement to the spiral center along the printing steps, indicating the CL scaffolds well supported the adhesion of rBMSCs. For the further cell adhesion and delivery experiment (movie S13), the images of cells after cultured for 24 h were taken by CLSM. As shown in Fig. 4A. The distribution density of rBMSCs in the CL scaffolds was gradually enhanced with the increase of pitches. Moreover, the 3D reconstruction images of CLSM showed that the rBMSCs in the CL groups were periodically distributed in spiral ladders, and the cytoskeleton tended to be arranged

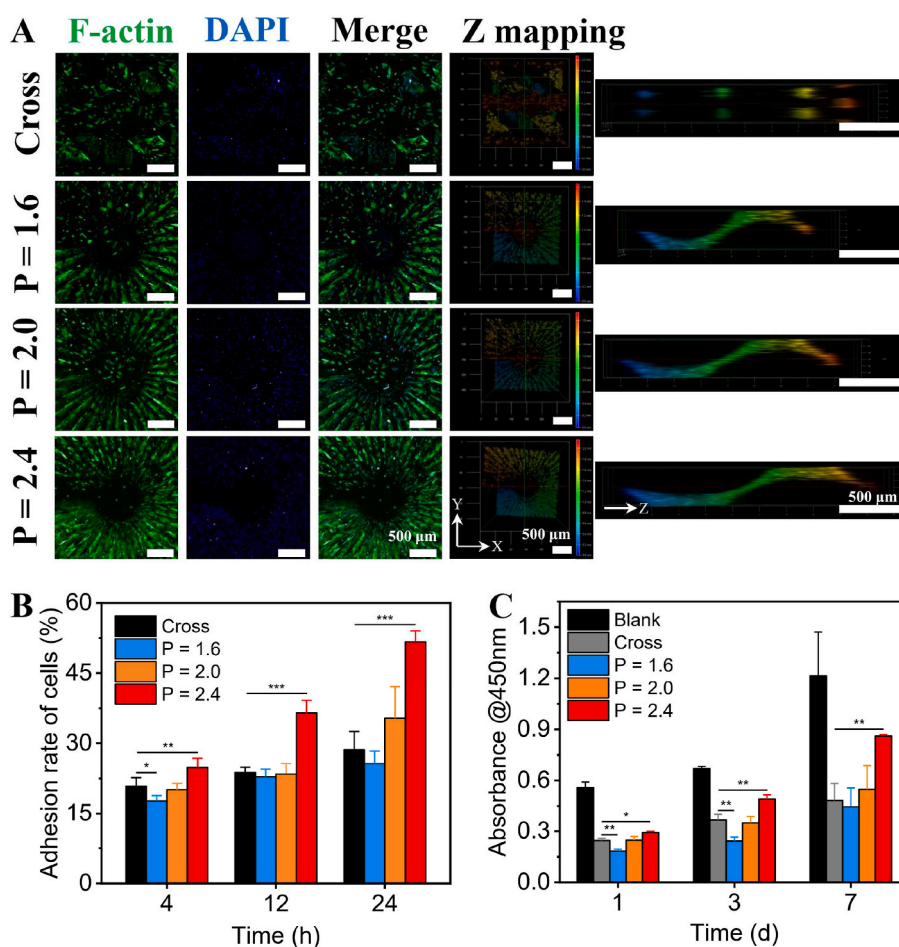


**Fig. 4.** Adhesion and proliferation activities of rBMSCs in the 3D-printed CL scaffolds with varied pitches. (A) CLSM images of rBMSCs adhered on the scaffolds after cultured for 24 h, scale bars = 500  $\mu$ m. (B) Quantitative analysis of rBMSCs adhered on the scaffolds after cultured for 4, 12 and 24 h, respectively ( $n = 6$ ). (C) The proliferation activity of rBMSCs in the scaffolds after cultured for 1, 3 and 7 days, respectively ( $n = 3$ ). (\* $P < 0.05$ , \*\* $P < 0.01$ , \*\*\* $P < 0.001$ ).

along the printing steps. On the contrary, rBMSCs in the Cross group were distributed discretely with no obviously oriented arrangement (Figs. S7A–D). The semicircular polar diagrams and quantitative analysis of the orientation angle of rBMSCs adhered on the different scaffolds further showed that the rBMSCs adhered on the CL scaffolds were more orderly aligned along the printing steps with the pitches increasing, while rBMSCs adhered on the Cross group were no obviously oriented arrangement (Figs. S7E–I). Furthermore, as shown in Fig. S8, in the cell adhesion and delivery assay, the absorption value at 450 nm of the incubation solution of cell counting kit-8 (CCK-8) had a good linearity linear relationship with the number of cells. Therefore, the relative adhesion rate of rBMSCs after cultured for 4, 12 and 24 h for the CL scaffolds was quantitatively analyzed by CCK-8 method. The results indicated that the initial adhesion rate of the seeded rBMSCs in the CL scaffolds exhibited positive correlation with pitch and culture time (Fig. 4B). Especially, the cell adhesion rate of CL scaffolds reached  $51.69 \pm 2.34\%$  at 24 h, increasing around 0.8 times than that of the Cross scaffolds ( $28.65 \pm 3.88\%$ ).

Supplementary data related to this article can be found at <https://doi.org/10.1016/j.bioactmat.2022.09.014>.

These may credit to the structure and porosity of the scaffolds. Previous studies mostly showed that the number of cells adhered on the scaffolds is largely affected by the surface area of scaffolds [47,48]. However, it was obvious that with the increase of pitches, the porosity of the CL scaffolds gradually increased. The higher porosity made the suspended rBMSCs easier to penetrate into the CL scaffolds. Consequently, the cell delivery efficiency of the scaffolds was improved. Besides, compared to the conventional scaffolds with discrete cross-strut structure, the CL scaffolds were conducive to loading the suspended rBMSCs because of the consecutive spiral structure. Live/dead staining assay was conducted to evaluate the viability of rBMSCs seeded in the CL scaffolds. As shown in Fig. S9. The rBMSCs seeded in the CL scaffolds maintained high viabilities, indicating that the CL scaffolds had good biocompatibility and no obvious cytotoxicity. Moreover, the results of cell proliferation test (movie 14) suggested that the proliferation activity of rBMSCs in the CL scaffolds was gradually enhanced with the increase of pitches (Fig. 4C). Similarly, the high porosity of the CL scaffolds, coupled with the open spiral structure, has been proved to possess excellent liquid transport performance (Fig. S5), may be also beneficial for improving the transmission of oxygen and nutrients. Therefore, with the increasing of pitches, the delivery of oxygen and nutrients may be increased, and the CL scaffolds could obviously have enhanced cell proliferation activity [27,49,50]. In addition, due to the layer-by-layer curing mode of DLP 3D printing, the spiral structure with stepped characteristic similar to stairs was produced in the CL scaffolds. This “stair-like” morphology of the scaffolds can mediate the actin, vinculin, and fibronectin expression of loaded cells, thus affecting their adhesion and proliferation ability on scaffolds [38,51–54]. Overall, these results demonstrated the improved cell delivery efficiency of the CL scaffolds. The CL scaffolds with 3D spiral structure well supported adhesion and proliferation of the cells, and had good biocompatibility, which could be applied for efficient cell delivery in bone tissue regeneration.

Supplementary video related to this article can be found at <https://doi.org/10.1016/j.bioactmat.2022.09.014>.

### 3.3. Cell migration assay *in vitro*

Previous studies showed that one of the key strategies of tissue repair is to guide appropriate cells to migrate to the target site [20,47]. We supposed that the biomimetic CL scaffolds with spiral structure would guide and facilitate the directional migration of rBMSCs. Therefore, the migration capability of rBMSCs in the CL scaffolds was investigated (movie S14). The rBMSCs were seeded to the bottom of scaffolds through the cell seeding channel in the peripheral wall, so as to evaluate the migration of rBMSCs in 10 days. Firstly, CLSM was used to image the scaffolds after cultured for 1 day to determine the initial position of

seeded rBMSCs (marked by yellow dotted lines) (Fig. 5A–D). And the scaffolds after cultured for 10 days were also imaged to determine the final position of rBMSCs after migrating (marked by yellow solid lines) (Fig. 5E–H, I–L). Specifically, the initial position of seeded rBMSCs was around at the bottom of each layer (indicated by red solid lines) for the CL groups and the third layer (L3) for the Cross group. The migration capabilities of rBMSCs in Z direction (vertical direction) and XY direction (horizontal direction) were statistically analyzed by number change of printing steps and angle change between the initial position and the final position, respectively (Fig. 5M and N). Fig. 5 showed that benefiting from the biomimetic spiral structure of the CL scaffolds, the migration obstruction of rBMSCs was relieved. The spiral sections in the CL scaffolds could act as the stairs to support cells migrating along Z direction. With the increase of pitches, rBMSCs in the CL scaffolds migrated upward more easily along Z direction (Fig. 5B–D, F–H). Quantitative statistics further suggested that the migration capability of the CL scaffolds in Z direction was gradually enhanced with the increase of pitches, and the CL scaffolds with  $P = 2.4$  mm exhibited the optimal effect on cell migration (Fig. 5M). The migration capability in XY direction showed a similar trend (Fig. 5N). In contrast, the migration of rBMSCs along Z direction in Cross scaffolds group was constrained. Most of rBMSCs in the Cross scaffolds only migrated on the horizontal plane of struts (Fig. 5A, E, M, and N). Thus, the CL scaffolds significantly enhanced the migration capability of rBMSCs along Z direction, showing a great potential to guide the endogenous stem cells to directionally migrate from the proximal part to the distal part. Besides, the rBMSCs in the CL scaffolds were highly aligned along the direction of printing steps, while the rBMSCs in the Cross scaffolds exhibited a disordered arrangement (Fig. 5I–L, Fig. S6, Fig. S7 and Fig. S10). The semicircular polar diagrams and quantitative analysis of the orientation angle of rBMSCs adhered on the different scaffolds after migrating for 10 days (in Fig. 5I–L) further showed a similar trend (Fig. S10) that the rBMSCs adhered on the CL scaffolds were more orderly aligned along the printing steps with the pitches increasing, while rBMSCs adhered on the Cross group were relatively more disordered. Therefore, the CL scaffolds showed advantages of controlling the distribution of rBMSCs, which might have a positive effect on the osteogenic differentiation [55–58].

For the results of cell migration assay, this might be caused by the cohesive migration of rBMSCs populations in the CL scaffolds. In cell migration assay, rBMSCs with a high density were seeded near the bottom of different scaffolds (i.e., initial position, Fig. 5A–D). Contact inhibition and contact stimulation of migration [59,60], might cause rBMSCs spread on the printing step at the initial position of cell seeded, and completely cover the surface of the printing step finally. After that, the unique spiral structure with stepped characteristic of the CL scaffolds might reduce the difficulty of the movement and migration of rBMSCs, which is similar to the role of steps in the stairs. So that a small part of the rBMSCs at the initial position could continue to migrate to the printing step of the upper layer through the cohesive migration of cell populations in the CL scaffolds. Then they gradually covered the printing step of the upper layer, and cause the rBMSCs contact each other. Subsequently, a small part of rBMSCs migrate to the upper printing step again. Finally, the effect of directional migration along the Z direction appeared in the spiral structure with stepped characteristic of the CL scaffolds by the procedure of this cycle (Fig. 5F–H). With the pitches increasing, rBMSCs could migrate higher and farther in the same time period (10 days) in the CL scaffolds, compared with the CL scaffolds with smaller patches and the Cross group (Fig. 5F–H, M–N). On the one hand, for the CL scaffolds, the width of printing step (i.e., the angle corresponding to each printing step) gradually decreased with the increase of pitches (Fig. 2B3–D3), and the time of covering a layer of printing steps would correspondingly decrease theoretically. On the other hand, rBMSCs also tended to be arranged orderly along the direction of the printing steps (Fig. 5J–L, and Fig. S10) with the pitches increasing, and the cytoskeleton of rBMSCs was elongated, which might be beneficial to the diffusion and spreading of rBMSCs in each printing step by

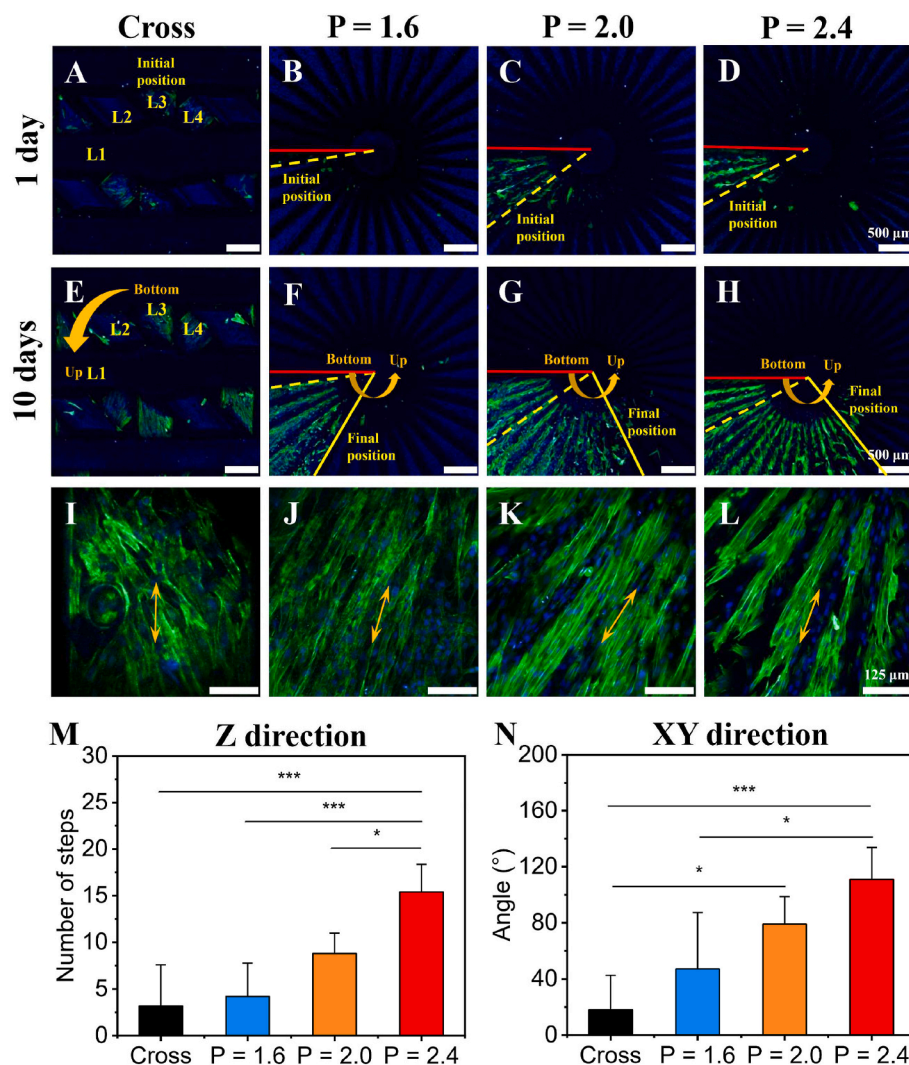


**Fig. 5.** Migration capability of rBMSCs in the 3D-printed CL scaffolds with varied pitches (serum content: 5%). (A–D) The representative CLSM images of the initial position (marked by yellow dotted lines) of rBMSCs after cultured for 1 day, scale bars = 500  $\mu\text{m}$ . (The red solid lines represented the bottom position of spiral circle in the CL scaffolds.) (E–H) The representative CLSM images of the final position (marked by yellow solid lines) of rBMSCs after migrating for 10 days, scale bars = 500  $\mu\text{m}$ . (I–L) The corresponding magnified CLSM images of rBMSCs after migrating for 10 days, scale bars = 125  $\mu\text{m}$ . Statistical analysis of cell migration in Z direction (vertical direction) (M) and XY direction (horizontal direction) (N). ( $n = 5$ ,  $*P < 0.05$ ,  $***P < 0.001$ ). Yellow arrows showed the direction of a single strut for the conventional cross-strut scaffolds or a printing step for the CL scaffolds.

improving the internal tension of the actomyosin cytoskeleton of rBMSCs. Because most of animal cells were related on the dynamics of the actomyosin cytoskeleton for motion [59]. These two factors together led to the more rapidly continuous directional migration of rBMSCs along the spiral structure with stepped characteristic of the CL scaffolds with the increase of pitches. In contrast, since the traditional Cross scaffolds did not have such a transitional structure similar to the spiral structure with stepped characteristic of the CL scaffolds in the Z direction, rBMSCs seeded at the initial addition position could only migrate on the horizontal surface of the solid struts, and migrate to the lower position of the Cross scaffolds under the action of natural gravity. And it was hard for rBMSCs in the Cross scaffolds to migrate from the low position of the Cross scaffolds to the higher position of the struts by anti-gravity as rBMSCs in the CL scaffolds.

Under conventional culture conditions (10% serum), when rBMSCs were cultured in the varied scaffolds for 10 days, they could both proliferate and migrate in the scaffolds. Therefore, in the previous cell scratch migration assays on two-dimensional plates, in order to exclude the influence of cell proliferation, the cell migration assay can be carried out in a medium without serum or containing no more than 1% serum, but usually no longer than 24 h [20]. Considering that in a relatively long period of 10 days in this work, if such a low serum concentration culture condition is still used for cell culture in the cell migration assays, it is undoubtedly unfavorable to maintain the normal state of the seeded rBMSCs. Consequently, in the cell migration assay (within 10 days), the

medium with low serum concentration (5% serum, only half of the conventional experiment) was conservatively selected for the experiment to weaken the influence of cell proliferation on migration as far as possible. Moreover, in this study, since the Cross group was also cultured under the same conditions as control, the influence of cell proliferation could be ignored. It is suggested that the structure of scaffolds plays an important role for cell migration.

#### 3.4. Cell osteogenic differentiation assay *in vitro*

Subsequently, to investigate the effect of CL scaffolds on osteogenic differentiation of rBMSCs (movie S14), quantitative reverse transcription PCR (RT-qPCR) technology was used to quantify the expression levels of bone-related genes: BSP, OCN, Runx2, BMP2 and OPN (Fig. 6A–E). Generally, compared to the Blank and Cross groups, the CL scaffolds with  $P = 2.0$  and  $2.4$  mm significantly enhanced the expression of osteogenic relative genes in rBMSCs for 7 days. Moreover, alizarin red S (ARS) staining assay was performed to evaluate the osteogenic differentiation of BMSCs in the CL scaffolds *in vitro* (Fig. S11). On account of that simple bioceramic scaffolds with no rBMSCs seeded were inevitable to be stained by ARS dyes (Fig. S11A<sub>1</sub>-D<sub>1</sub>), the absorbance values of the simple ceramic scaffolds without cells seeded were respectively deducted from those of the scaffolds with cells seeded to exclude the effect of the dye absorption of the scaffolds themselves. The digital photographs (Fig. S11A<sub>2</sub>-D<sub>2</sub>) and the corresponding quantitative

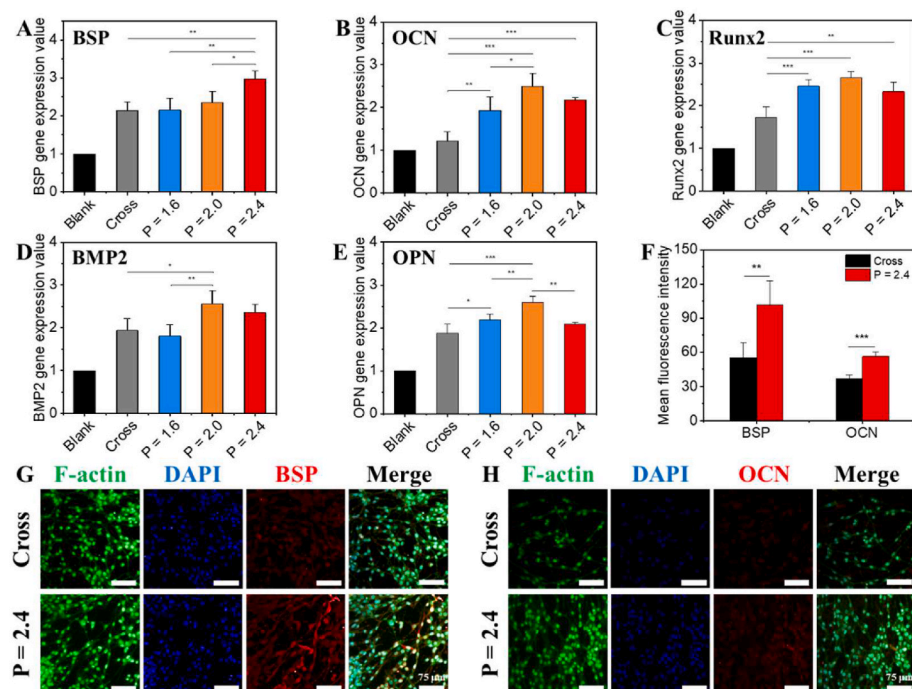


**Fig. 6.** The osteogenic differentiation of rBMSCs in the 3D-printed CL scaffolds with varied pitches after cultured for 7 days *in vitro*. (A–E) Quantitative expression of relative osteogenic genes: BSP (A), OCN (B), Runx2 (C), BMP2 (D) and OPN (E) of rBMSCs cultured in different scaffolds for 7 days ( $n = 4$ ). (F) The semi-quantitative analysis of BSP and OCN proteins expression ( $n = 3$ ). (G, H) CLSM images of immunofluorescence staining of relative osteogenic proteins: BSP (G) and OCN (H), scale bars = 75  $\mu\text{m}$ . (\* $P < 0.05$ , \*\* $P < 0.01$ , \*\*\* $P < 0.001$ ).

analysis (Fig. S11E) results indicated that the  $P = 2.4$  group possessed the best osteogenic differentiation effect as compared with Cross,  $P = 1.6$  and  $P = 2.0$  group. And calcium deposition within rBMSCs in the scaffolds had much higher density with deeper red color as compared to the scaffolds themselves. Therefore, it was believed that the CL scaffolds promoted the osteogenic differentiation of rBMSCs. Considering the fact that the CL scaffolds with  $P = 2.4$  mm performed better in cell adhesion, proliferation and migration, the CL scaffolds with  $P = 2.4$  mm were selected for further immunofluorescence testing. As shown in Fig. 6F–H. The semi-quantitative statistical analysis and images of immunofluorescent protein staining further confirmed that both the expression levels of early osteogenic marker BSP and late osteogenic marker OCN of rBMSCs in the CL scaffolds were obviously improved as compared to those in the Cross scaffolds.

These results indicated that the CL scaffolds could substantially improve the osteogenic differentiation activity of the cells. It might be because of the special spiral structure of the CL scaffolds. On the one hand, the CL scaffolds with  $P = 2.4$  mm were beneficial to the transmission of nutrition and constructed a proper microenvironment to promote the osteogenic differentiation of rBMSCs. Besides, as the rBMSCs were aligned along the printing steps, which was contributed to the osteogenic differentiation [50,51]. Previous studies found that surface topography could regulate osteogenic differentiation of MSCs *via* crosstalk between FAK/MAPK and ILK/ $\beta$ -catenin pathways [61]. In addition, the macro-microstructure would influence the tension of intracellular skeleton, and then activate signaling pathways such as Runx2, Wnt, to stimulate osteogenic differentiation [49,53,55,62].

Furthermore, since the composition of the CL scaffolds was well degradable  $\beta$ -TCP material, which contained two bioactive ions, calcium ions ( $\text{Ca}^{2+}$ ) and phosphate ions ( $\text{P}_i$ ). The different 3D structure and surface morphology of scaffolds might affect the two ions release of scaffolds. Therefore, we further tested the Ca and  $\text{P}_i$  ions released behavior of the CL scaffolds in the culture medium according to the inductively coupled plasma atomic emission spectroscopy (ICP-AES) (Fig. S12). The results showed that, there was no significant difference for  $\text{Ca}^{2+}$  levels among the CL scaffolds with varied pitches in 7 days. Moreover, there was no large difference for  $\text{Ca}^{2+}$  levels between the CL scaffolds and the Cross group. Only in the initial stage,  $\text{Ca}^{2+}$  ions

released from the CL scaffolds with  $P = 2.0$  mm at 1 and 3 days, and the CL scaffolds with  $P = 2.4$  mm at 1 day, were slightly increased with statistical difference as compared to the Cross group. Previous studies have shown that the dissolved  $\text{Ca}^{2+}$  ions released from the surface of calcium phosphate bioceramics seem to play an important role in influencing cell osteogenic differentiation, which can promote osteogenic differentiation *via* the ERK1/2 pathway [38]. Consequently, in addition to the structural factors of the CL scaffolds themselves, the slight increase in the concentration of  $\text{Ca}^{2+}$  ions released from the CL scaffolds in the initial stage might be another main reason that the CL scaffolds with  $P = 2.0$  mm and  $2.4$  mm significantly promoted the osteogenic differentiation of rBMSCs. Moreover, we also tested the release of  $\text{P}_i$  ions. The results showed that there was no significant difference between the CL scaffolds and the Cross group in the early 1 and 3 days. But the CL scaffolds with  $P = 1.6$  mm and  $P = 2.0$  mm showed a significant difference in  $\text{P}_i$  ions release levels as compared to the Cross group at 5 and 7 days, and the  $\text{P}_i$  ion release concentration was significantly increased. While the CL scaffolds with  $P = 2.4$  mm showed a slight increase in  $\text{P}_i$  ions release levels as compared to the Cross group at 1, 3, 5 and 7 days with no significant difference. This trend (at 5 and 7 days) was similar to the expression level of OPN gene in RT-qPCR experiment, indicating that the higher release level of  $\text{P}_i$  ion in late stage also had a positive effect on osteogenic differentiation of rBMSCs. Previous studies have showed that phosphate appeared to play only a secondary role in aiding osteogenic differentiation in contrast to the role played by  $\text{Ca}^{2+}$ . And phosphate could induced elevation of OPN gene *via* the activation of ERK1/2- and PKC-dependent pathways, while  $\text{Ca}^{2+}$  was required for phosphate to activate ERK1/2-dependent pathways [63]. The above results indicated that the unique structure of the CL scaffold did cause slightly difference in  $\text{Ca}^{2+}$  and  $\text{P}_i$  ions released from the scaffolds as compared to the Cross group, and might influence the osteogenic differentiation of rBMSCs, which may be not the main factor.

### 3.5. Bioactivity experiments *in vivo*

After verifying the *in vitro* bioactivity of the CL scaffolds *in vitro*, we developed a half-embedded femoral defect of rabbit model to investigate the directional bone growth *in vivo*. Three groups were prepared: Blank,

Cross scaffolds and CL scaffolds with  $P = 2.4$  mm (movie S15). As shown in Fig. 7 and Fig. S13, part of the implanted scaffolds was protruded out of the defects. The digital photograph of the samples suggested that there was no obvious inflammatory reaction in defects for each group, and the implanted scaffolds were integrated well with the surrounding bone tissue (Fig. 7A1-F1, A2-F2). In addition, as shown in the images reconstructed by Micro-CT, more new bone tissue (green) was obviously formed in the CL scaffolds at 8 and 12 weeks, especially in the spiral cavity of scaffolds, than that in other two groups, indicating that the CL scaffolds demonstrated the improved ability of inducing bone regeneration *in vivo* (Fig. 7A3-F3, A4-F4, and A5-F5). Furthermore, the new bone tissue in the CL scaffolds was decreasingly formed from the bottom to top of scaffolds at 8 weeks, while the new bone tissue in the CL scaffolds was uniformly formed from the bottom to top of scaffolds at 12 weeks. Interestingly, there was more new bone regenerated in the protruded part of the CL scaffolds at 12 weeks compared to that at 8 weeks. In contrast, only a little new bone formed in the conventional Cross scaffolds at 8 and 12 weeks, especially less in the protruded part. The results indicated that the new bone tissue in the CL scaffolds was gradually

growing along the spiral structure from the bottom to top of scaffolds, which was like “climbing stairs”. Micro-CT statistical analysis further suggested that the overall new formed bone volume to the total volume (BV/TV) ratio (Fig. 7G), and the new trabecular number (Tb. N) (Fig. 7H) of the CL scaffolds were significantly higher than that of the Blank and the Cross group at 8 and 12 weeks. For the embedded part, the BV/TV ratio (Fig. S14A) and Tb. N (Fig. S14B) of the CL scaffolds were higher than those of the Cross group for the embedded part at 8 and 12 weeks. And there was a significant difference at 8 weeks, while there was no significant difference at 12 weeks. Especially, the BV/TV ratio of the protruded part (Fig. 7I) of the CL group (~2.5 mm, above the red dotted line in Fig. 7A5-F5) was generally higher than that of the Cross group at 8 weeks, and obviously higher than that of the Cross group at 12 weeks. It suggested that the CL scaffolds were able to promote guiding directional bone regeneration as time goes on.

Supplementary data related to this article can be found at <https://doi.org/10.1016/j.bioactmat.2022.09.014>.

To further evaluate the bone regeneration effect of the CL scaffolds *in vivo*, the histological analysis with Van Gieson’s picrofuchsin (VG)

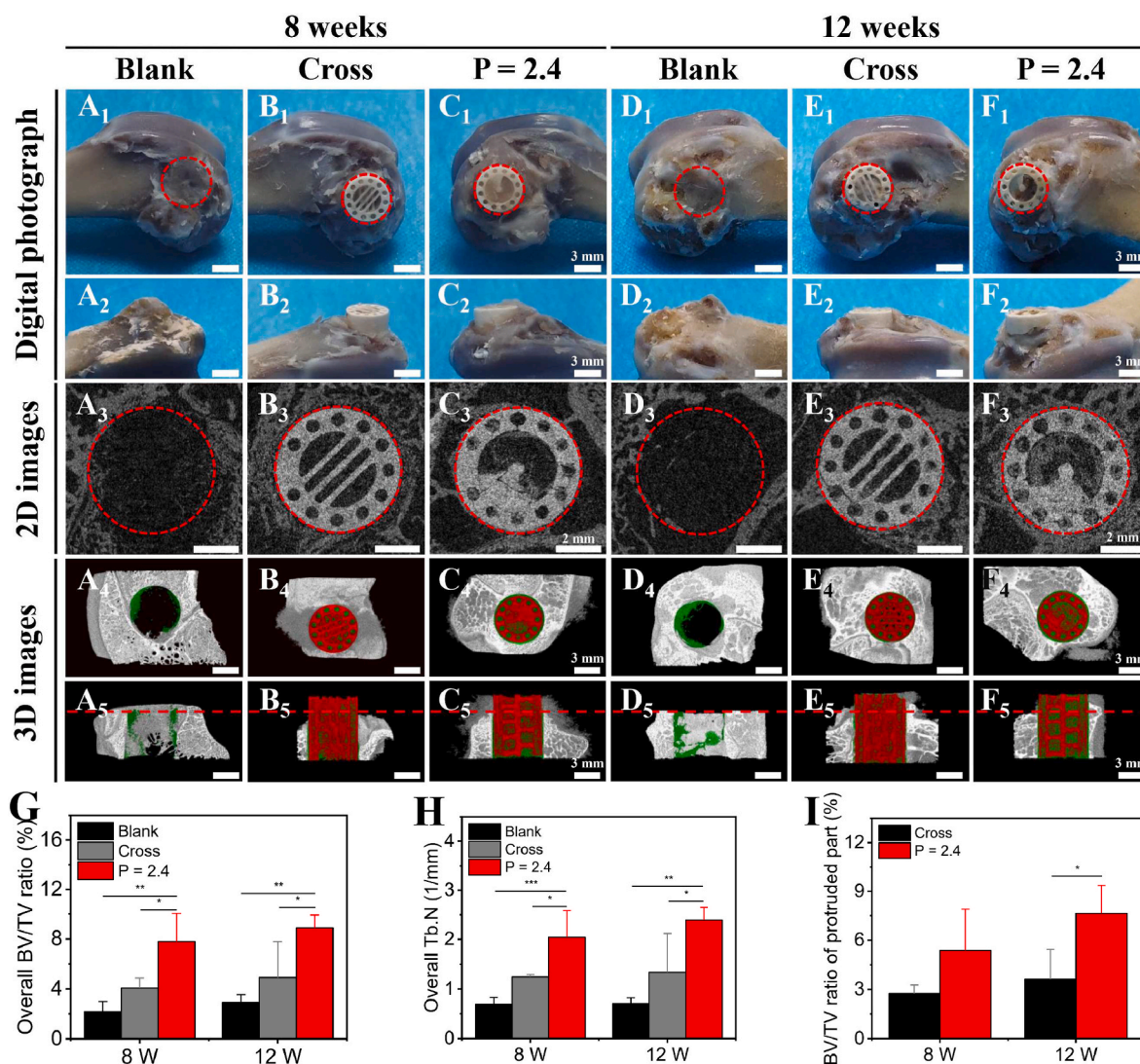


Fig. 7. The *in vivo* bone regeneration of the 3D-printed CL scaffolds in the half-embedded rabbit femoral defects. Digital photograph (A1-F1, A2-F2) (A1-F1: vertical view, and A2-F2: side view), 2D Micro-CT images (A3-F3) and 3D Micro-CT reconstruction images (A4-F4, A5-F5) (A4-F4: transverse view, and A5-F5: sagittal view; the green, red and white color in 3D Micro-CT images represented newly formed bone, scaffolds and primary bone, respectively) of the femoral defects after operated for 8 and 12 weeks in the three groups. The red dotted line indicated the protruded part of the implanted scaffolds, scale bars = 3, 3, 2, 3, 3 mm, respectively. (G-I) Micro-CT reconstruction analysis. The overall newly formed bone volume to the total volume (BV/TV) ratio (G), the overall new trabecular number (Tb. N) (H), and the BV/TV ratio of the protruded part (I) at 8 and 12 weeks. (n = 4, \* $P < 0.05$ , \*\* $P < 0.01$ , \*\*\* $P < 0.001$ ).

staining was performed. As shown in Fig. 8. A little new bone tissue formed in the Blank group at 8 and 12 weeks, which was only found on the periphery of the defects (Fig. 8A and D). For the implanted scaffolds, more new bone tissue was induced, especially in the embedded part of the CL scaffolds (Fig. 8C and F). Moreover, the embedded parts for the two kinds of scaffolds were closely integrated with the growing peripheral bone tissue, indicating the good biocompatibility and osteointegration of the bioceramic materials (Fig. 8B<sub>1</sub>, C<sub>1</sub>, E<sub>1</sub>, and F<sub>1</sub>). Notably, for the embedded part, the CL scaffolds obviously induced more newly formed bone tissue than the conventional Cross scaffolds at 8 and 12 weeks. What's more, the new bone tissue was mostly distributed in the spiral cavities and on the surface of spiral sections in the CL scaffolds, while it was only distributed on the surface of struts with less content in the Cross scaffolds (Fig. 8B, C, E, and F). Besides, considerable new bone tissue was observed in the through macropores of the scaffolds. Similarly, for the protruded part of scaffolds, there was only a little new bone tissue formed in the Cross scaffolds at 8 and 12 weeks, no matter on the surface of struts or in the through macropores (Fig. 8G and I). In comparison, the CL scaffolds obviously guided more newly formed bone growing to the top of the scaffolds compared with the Cross scaffolds at 8 and 12 weeks (Fig. 8H and J). A large amount of new bone tissue was formed in the spiral cavity of the protruded part in the CL scaffolds at 12 weeks.

These results suggested that the CL scaffolds with spiral structure

demonstrated better effect on bone regeneration and could well guide the directional bone growth from the bottom to top of scaffolds with time prolonging. This might be attributed to the special spiral structure of the CL scaffolds. Previous studies had shown that the macro and micro structures of biomaterials would significantly affect the behaviors of stem cells [62]. Introducing different natural biomimetic structures into bone tissue engineering scaffolds would exhibit varied effects on cell behavior and tissue regeneration, such as the lotus root-like biomimetic materials, hot dog-like biomaterials, and Haversian bone-mimicking scaffolds [64–66]. For the CL scaffolds, with the spiral structure, the scaffolds could well guide and promote the migration of endogenous rBMSCs from the bottom to the top of scaffolds, and enhance the subsequent proliferation as well as osteogenic differentiation. Besides, ideal bone tissue engineering scaffolds should be interconnected to ensure the effective exchange of oxygen and nutrients in the bone formation process [13,22,24–26]. The open architecture of the CL scaffolds could well improve the interconnectivity, the transmission of nutrients and the in-growth of new bone tissue, which may collectively promote the directional growth of bone tissue guided by CL scaffolds from the proximal part to the distal part. However, it should be pointed out that osteoblast differentiation study has not been conducted *in vivo* experiments, which should be further investigated for such implanted bioceramic scaffolds in the future research. Moreover, considering the significant differences in physiological conditions *in vivo* and *in vitro*, cell

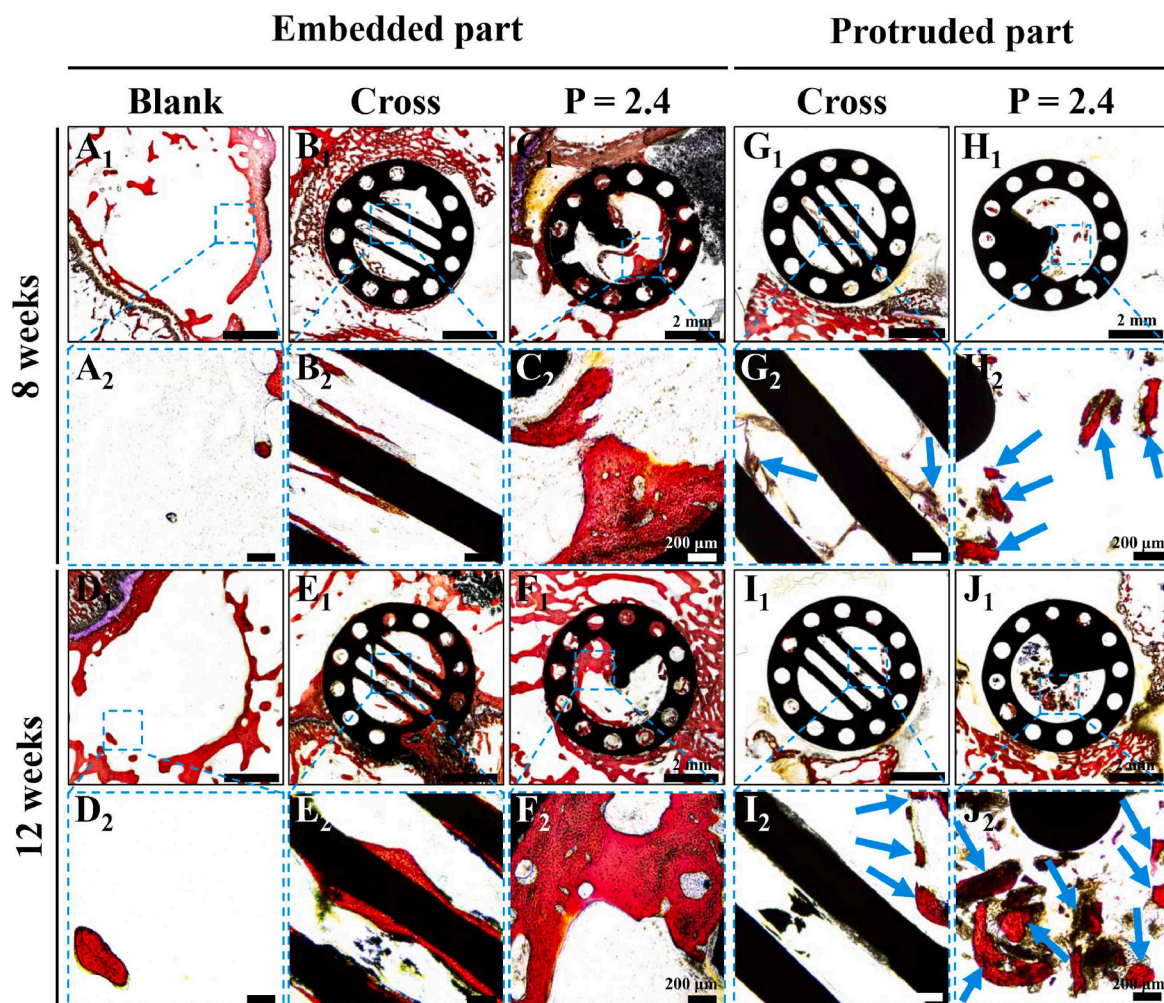


Fig. 8. Histological analysis to evaluate the new bone formation in both embedded and protruded part of the CL scaffolds after implanted for 8 and 12 weeks. (A<sub>1</sub>-F<sub>1</sub>) VG staining images of the embedded parts after 8 (A<sub>1</sub>-C<sub>1</sub>) and 12 (D<sub>1</sub>-F<sub>1</sub>) weeks of operation, scale bars = 2 mm. (G<sub>1</sub>-J<sub>1</sub>) VG staining images of the protruded parts after 8 (G<sub>1</sub>, H<sub>1</sub>) and 12 (I<sub>1</sub>, J<sub>1</sub>) weeks of operation, scale = 2 mm. (A<sub>2</sub>-J<sub>2</sub>) Magnified images of the marked region in A<sub>1</sub>-J<sub>1</sub>, scale bars = 200 μm. Red for new bone, black for scaffolds, and blue arrows evidently pointed to the newly formed bone tissue.

behaviors *in vivo* such as migration and proliferation also need to be further studied in future work.

#### 4. Conclusion

In summary, we successfully prepared the CL bioceramic scaffolds with spiral structure through DLP-based 3D printing technology, which showed great potential for guiding the directional bone growth. Firstly, the morphology, structure, porosity and mechanical properties of the scaffolds could be flexibly and accurately controlled by model design. Secondly, compared with the conventional cross-strut scaffolds, the CL scaffolds could improve material transport ability and enhance the biological behaviors of seeded rBMSCs including adhesion, proliferation and osteogenic differentiation in a pitch-dependent manner. Particularly, the CL scaffolds could guide the cells to migrate along the vertical direction, which was like “cells climbing stairs”. Moreover, the scaffolds well guided the bottom-up directional bone growth and enhanced bone regeneration *in vivo*. Therefore, our study suggested that the 3D-printed CL scaffolds would be a promising candidate for repairing severe bone defects, and even limbs. Furthermore, this study offered a promising strategy for the design and manufacture of biomimetic materials for complex tissue regeneration.

#### Ethics approval and consent to participate

We further confirm that any aspect of the work covered in this manuscript that involving experimental animals has been conducted with the ethical approval of Institutional Animal Care and Use Committee of Nanjing First Hospital, Nanjing Medical University.

#### CRediT authorship contribution statement

**Boshi Feng:** Conceptualization, Investigation, Methodology, Formal analysis, Visualization, Validation, Writing – original draft. **Meng Zhang:** Investigation, Methodology, Formal analysis, Resources. **Chen Qin:** Investigation, Writing – review & editing. **Dong Zhai:** Methodology, Formal analysis, Resources. **Yufeng Wang:** Methodology, Resources. **Yanling Zhou:** Resources, Funding acquisition. **Jiang Chang:** Supervision. **Yufang Zhu:** Supervision. **Chengtie Wu:** Conceptualization, Supervision, Project administration, Writing – review & editing, Funding acquisition.

#### Declaration of competing interest

The authors declare that they have no known competing financial interests or personal relationships that could have appeared to influence the work reported in this paper.

#### Acknowledgements

This work was supported by the National Key Research and Development Program of China (grant number 2021YFB3800800); the Natural Science Foundation of China (grant numbers 32225028, 32130062); Science and Technology Commission of Shanghai Municipality (grant number 21DZ1205600); Shanghai Pilot Program for Basic Research-Chinese Academy of Science, Shanghai Branch (grant number JCYJ-SHFY-2022-003).

#### Appendix A. Supplementary data

Supplementary data to this article can be found online at <https://doi.org/10.1016/j.bioactmat.2022.09.014>.

#### References

- [1] M.R. Iaquinta, E. Mazzoni, I. Bononi, J.C. Rotondo, C. Mazziotta, M. Montesi, S. Sprio, A. Tampieri, M. Tognon, F. Martini, Adult stem cells for bone regeneration and repair, *Front. Cell Dev. Biol.* 7 (2019) 268.
- [2] H. Petite, V. Viateau, W. Bensaid, A. Meunier, C. de Pollak, M. Bourguignon, K. Oudina, L. Sedel, G. Guillemin, Tissue-engineered bone regeneration, *Nat. Biotechnol.* 18 (9) (2000) 959–963.
- [3] A.M. McDermott, S. Herberg, D.E. Mason, J.M. Collins, H.B. Pearson, J. H. Dawahare, R. Tang, A.N. Patwa, M.W. Grinstaff, D.J. Kelly, E. Alsborg, J. D. Boerckel, Recapitulating bone development through engineered mesenchymal condensations and mechanical cues for tissue regeneration, *Sci. Transl. Med.* 11 (495) (2019), eaav7756.
- [4] R. Cancedda, P. Giannoni, M. Mastrogiacomo, A tissue engineering approach to bone repair in large animal models and in clinical practice, *Biomaterials* 28 (29) (2007) 4240–4250.
- [5] B. Dalisson, B. Charbonnier, A. Aoude, M. Gilardino, E. Harvey, N. Makhoul, J. Barralet, Skeletal regeneration for segmental bone loss: vascularised grafts, analogues and surrogates, *Acta Biomater.* 136 (2021) 37–55.
- [6] Q. Jiang, K. Huang, Y.Y. Liu, G.Y. Chi, Using the Ilizarov technique to treat limb shortening after replantation of a severed lower limb: a case report, *Ann. Transl. Med.* 8 (16) (2020) 1025.
- [7] G.S. Xu, L. Gao, K. Tao, S.X. Wan, Y.N. Lin, A. Xiong, B. Kang, H. Zeng, Three-dimensional-printed upper limb prosthesis for a child with traumatic amputation of right wrist: a case report, *Medicine* 96 (52) (2017), e9426.
- [8] A.Y. Shi, A. Heinayati, D.Y. Bao, H.F. Liu, X.C. Ding, X. Tong, L.D. Wang, B. Wang, H.Y. Qin, Small molecule inhibitor of TGF- signaling enables robust osteogenesis of autologous GMSCs to successfully repair minipig severe maxillofacial bone defects, *Stem Cell Res. Ther.* 10 (2019) 172.
- [9] M. Ronga, M. Cherubino, K. Corona, A. Fagetti, B. Bertani, L. Valdatta, R. Mora, P. Cherubino, Induced membrane technique for the treatment of severe acute tibial bone loss: preliminary experience at medium-term follow-up, *Int. Orthop.* 43 (1) (2019) 209–215.
- [10] C.W. Hartman, CORR insights(A (R)): modular tapered implants for severe femoral bone loss in THA: reliable osseointegration but frequent complications, *Clin. Orthop. Relat. Res.* 473 (2) (2015) 561–562.
- [11] Y. Yamashita, I. Hashimoto, K. Goishi, Y. Fukunaga, Y. Abe, H. Nakanishi, Reconstruction of metatarsal bone defects with a free fibular osteomyocutaneous flap incorporating soleus muscle, *J. Plast. Reconstr. Aes.* 66 (2) (2013) 277–280.
- [12] E. Gomez-Barrena, P. Rosset, D. Lozano, J. Stanovici, C. Ermtaller, F. Gerbhard, Bone fracture healing: cell therapy in delayed unions and nonunions, *Bone* 70 (2015) 93–101.
- [13] S. Bose, S. Vahabzadeh, A. Bandyopadhyay, Bone tissue engineering using 3D printing, *Mater. Today* 16 (12) (2013) 496–504.
- [14] L. Zhang, G. Yang, B.N. Johnson, X. Jia, Three-dimensional (3D) printed scaffold and material selection for bone repair, *Acta Biomater.* 84 (2019) 16–33.
- [15] Y. Chen, W. Li, C. Zhang, Z. Wu, J. Liu, Recent developments of biomaterials for additive manufacturing of bone scaffolds, *Adv. Healthc. Mater.* 9 (23) (2020), 2000724.
- [16] N. Sarkar, S. Bose, Controlled release of soy isoflavones from multifunctional 3D printed bone tissue engineering scaffolds, *Acta Biomater.* 114 (2020) 407–420.
- [17] C. Yang, H. Ma, Z. Wang, M.R. Younis, C. Liu, C. Wu, Y. Luo, P. Huang, 3D printed wesselsite nanosheets functionalized scaffold facilitates NIR-II photothermal therapy and vascularized bone regeneration, *Adv. Sci.* 8 (20) (2021), 2100894.
- [18] F. Qu, F. Guilak, R.L. Mauck, Cell migration: implications for repair and regeneration in joint disease, *Nat. Rev. Rheumatol.* 15 (3) (2019) 167–179.
- [19] B. de Lucas, L.M. Perez, B.G. Galvez, Importance and regulation of adult stem cell migration, *J. Cell Mol. Med.* 22 (2) (2018) 746–754.
- [20] J. Xue, T. Wu, J. Qiu, S. Rutledge, M.L. Tanes, Y. Xia, Promoting cell migration and neurite extension along uniaxially aligned nanofibers with biomacromolecular particles in a density gradient, *Adv. Funct. Mater.* 30 (40) (2020), 2002031.
- [21] F. Karimi, A.J. O'Connor, G.G. Qiao, D.E. Heath, Integrin clustering matters: a review of biomaterials functionalized with multivalent integrin-binding ligands to improve cell adhesion, migration, differentiation, angiogenesis, and biomedical device integration, *Adv. Healthc. Mater.* 7 (12) (2018), 1701324.
- [22] D. Yang, Z. Zhao, F. Bai, S. Wang, A.P. Tomsia, H. Bai, Promoting cell migration in tissue engineering scaffolds with graded channels, *Adv. Healthc. Mater.* 6 (18) (2017), 1700472.
- [23] S.G. Pedrero, P. Llamas-Sillero, J. Serrano-López, A multidisciplinary journey towards bone tissue engineering, *Materials* 14 (17) (2021) 4896.
- [24] J.R. Jones, L.M. Ehrenfried, L.L. Hench, Optimising bioactive glass scaffolds for bone tissue engineering, *Biomaterials* 27 (7) (2006) 964–973.
- [25] M. Ye, P. Mohanty, G. Ghosh, Morphology and properties of poly vinyl alcohol (PVA) scaffolds: impact of process variables, *Mater. Sci. Eng. C* 42 (2014) 289–294.
- [26] E. Santos, R.M. Hernandez, J. Luis Pedraz, G. Orive, Novel advances in the design of three-dimensional bio-scaffolds to control cell fate: translation from 2D to 3D, *Trends Biotechnol.* 30 (6) (2012) 331–341.
- [27] V. Karageorgiou, D. Kaplan, Porosity of 3D biomaterial scaffolds and osteogenesis, *Biomaterials* 26 (27) (2005) 5474–5491.
- [28] J.F. Wang, Q.F. Cheng, Z.Y. Tang, Layered nanocomposites inspired by the structure and mechanical properties of nacre, *Chem. Soc. Rev.* 41 (3) (2012) 1111–1129.
- [29] W.R. Hansen, K. Autumn, Evidence for self-cleaning in gecko setae, *Proc. Natl. Acad. Sci. USA* 102 (2) (2005) 385–389.

- [30] H.W. Chen, T. Ran, Y. Gan, J.J. Zhou, Y. Zhang, L.W. Zhang, D.Y. Zhang, L. Jiang, Ultrafast water harvesting and transport in hierarchical microchannels, *Nat. Mater.* 17 (10) (2018) 935–942.
- [31] Z. Li, C. Chen, R. Mi, W. Gan, J. Dai, M. Jiao, H. Xie, Y. Yao, S. Xiao, L. Hu, A strong, tough, and scalable structural material from fast-growing bamboo, *Adv. Mater.* 32 (10) (2020), 1906308.
- [32] A. Velasco-Hogan, J. Xu, M.A. Meyers, Additive manufacturing as a method to design and optimize bioinspired structures, *Adv. Mater.* 30 (52) (2018), 1800940.
- [33] D.A. Chen, L.E. Klotz, B.E. Ross, Mathematically characterizing natural systems for adaptable, biomimetic design, *Procedia Eng.* 145 (2016) 497–503.
- [34] C.S. Tiwary, S. Kishore, S. Sarkar, D.R. Mahapatra, P.M. Ajayan, K. Chattopadhyay, Morphogenesis and mechanostabilization of complex natural and 3D printed shapes, *Sci. Adv.* 1 (4) (2015), e1400052.
- [35] L.-B. Mao, H.-L. Gao, H.-B. Yao, L. Liu, H. Colfen, G. Liu, S.-M. Chen, S.-K. Li, Y.-X. Yan, Y.-Y. Liu, S.-H. Yu, Synthetic nacre by pre-designed matrix-directed mineralization, *Science* 354 (6308) (2016) 107–110.
- [36] Y. Zhou, C. Wu, J. Chang, Bioceramics to regulate stem cells and their microenvironment for tissue regeneration, *Mater. Today* 24 (2019) 41–56.
- [37] L.L. Hench, Bioceramics, *J. Am. Ceram. Soc.* 81 (7) (1998) 1705–1728.
- [38] S. Samavedi, A.R. Whittington, A.S. Goldstein, Calcium phosphate ceramics in bone tissue engineering: a review of properties and their influence on cell behavior, *Acta Biomater.* 9 (9) (2013) 8037–8045.
- [39] L.L. Hench, J.M. Polak, Third-generation biomedical materials, *Science* 295 (5557) (2002) 1014–1017.
- [40] K.J.L. Burg, S. Porter, J.F. Kellam, Biomaterial developments for bone tissue engineering, *Biomaterials* 21 (23) (2000) 2347–2359.
- [41] R. Trombetta, J.A. Inzana, E.M. Schwarz, S.L. Kates, H.A. Awad, 3D printing of calcium phosphate ceramics for bone tissue engineering and drug delivery, *Ann. Biomed. Eng.* 45 (1) (2017) 23–44.
- [42] K. Lin, C. Wu, J. Chang, Advances in synthesis of calcium phosphate crystals with controlled size and shape, *Acta Biomater.* 10 (10) (2014) 4071–4102.
- [43] D.F. Silva, T.E. Friis, N.H.A. Camargo, Y. Xiao, Characterization of mesoporous calcium phosphates from calcareous marine sediments containing Si, Sr and Zn for bone tissue engineering, *J. Mater. Chem. B* 4 (42) (2016) 6842–6855.
- [44] Y.F. Gu, J. Zhang, X.Z. Zhang, G.P. Liang, T. Xu, W. Niu, Three-dimensional printed Mg-doped beta-TCP bone tissue engineering scaffolds: effects of magnesium ion concentration on osteogenesis and angiogenesis in vitro, *Tissue Eng. Regen. Med.* 16 (4) (2019) 415–429.
- [45] H. Goodarzi, S. Hashemi-Najafabadi, N. Baheiraei, F. Bagheri, Preparation and characterization of nanocomposite scaffolds (Collagen/beta-TCP/SrO) for bone tissue engineering, *Tissue Eng. Regen. Med.* 16 (3) (2019) 237–251.
- [46] J.M. Xue, H.S. Ma, E.H. Song, F. Han, T. Li, M. Zhang, Y.F. Zhu, J.J. Liu, C.T. Wu, Bamboo-based biomaterials for cell transportation and bone integration, *Adv. Healthc. Mater.* 11 (14) (2022), 2200287.
- [47] Y. Li, J. Xiong, P.D. Hodgson, C.e. Wen, Effects of structural property and surface modification of Ti6Ta4Sn scaffolds on the response of SaOS2 cells for bone tissue engineering, *J. Alloys Compd.* 494 (1) (2010) 323–329.
- [48] C. Wang, D.L. Xu, L. Lin, S.J. Li, W.T. Hou, Y. He, L.Y. Sheng, C. Yi, X.L. Zhang, H. Y. Li, Y.M. Li, W. Zhao, D.S. Yu, Large-pore-size Ti6Al4V scaffolds with different pore structures for vascularized bone regeneration, *Mater. Sci. Eng. C* 131 (2021), 112531.
- [49] Q.L. Loh, C. Choong, Three-dimensional scaffolds for tissue engineering applications: role of porosity and pore size, *Tissue Eng. Part B* 19 (6) (2013) 485–502.
- [50] M. Rumpfer, A. Woesj, J.W.C. Dunlop, J.T. van Dongen, P. Fratzl, The effect of geometry on three-dimensional tissue growth, *J. R. Soc. Interface* 5 (27) (2008) 1173–1180.
- [51] M.C. Siebers, P.J. ter Brugge, X.F. Walboomers, J.A. Jansen, Integrins as linker proteins between osteoblasts and bone replacing materials, A critical review, *Biomaterials* 26 (2) (2005) 137–146.
- [52] Y.W. Lim, S.Y. Kwon, D.H. Sun, H.E. Kim, Y.S. Kim, Enhanced cell integration to titanium alloy by surface treatment with microarc oxidation: a Pilot study, *Clin. Orthop. Relat. Res.* 467 (9) (2009) 2251–2258.
- [53] J. Manokawinchoke, P. Pavasant, C.N. Limjeerajarus, N. Limjeerajarus, T. Osathanon, H. Egusa, Mechanical loading and the control of stem cell behavior, *Arch. Oral Biol.* 125 (2021), 105092.
- [54] T. Ristori, A. Vigliotti, F.P.T. Baaijens, S. Loerakker, V.S. Deshpande, Prediction of cell alignment on cyclically strained grooved substrates, *Biophys. J.* 111 (10) (2016) 2274–2285.
- [55] J. Xie, H.Q. Shen, G.Y. Yuan, K.L. Lin, J.S. Su, The effects of alignment and diameter of electrospun fibers on the cellular behaviors and osteogenesis of BMSCs, *Mater. Sci. Eng. C* 120 (2021), 111787.
- [56] J. Xue, D. Pisignano, Y. Xia, Maneuvering the migration and differentiation of stem cells with electrospun nanofibers, *Adv. Sci.* 7 (15) (2020), 2000735.
- [57] L. Yang, L. Ge, Q. Zhou, T. Mokabber, Y. Pei, R. Bron, P. van Rijn, Biomimetic multiscale hierarchical topography enhances osteogenic differentiation of human mesenchymal stem cells, *Adv. Mater. Interfaces* 7 (14) (2020), 2000385.
- [58] X.S. Luo, S.Y. Zhang, B.H. Luo, H. Li, Engineering collagen fiber templates with oriented nanoarchitecture and concerns on osteoblast behaviors, *Int. J. Biol. Macromol.* 185 (2021) 77–86.
- [59] K.M. Yamada, M. Sixt, Mechanisms of 3D cell migration, *Nat. Rev. Mol. Cell Biol.* 20 (12) (2019) 738–752.
- [60] V. Hakim, P. Silberzan, Collective cell migration: a physics perspective, *Rep. Prog. Phys.* 80 (7) (2017), 076601.
- [61] H.Y. Niu, D. Lin, W. Tang, Y.F. Ma, B. Duan, Y. Yuan, C.S. Liu, Surface topography regulates osteogenic differentiation of MSCs via crosstalk between FAK/MAPK and ILK/beta-Catenin pathways in a hierarchically porous environment, *ACS Biomater. Sci. Eng.* 3 (12) (2017) 3161–3175.
- [62] D. Xiao, J. Zhang, C. Zhang, D. Barbieri, H. Yuan, L. Moroni, G. Feng, The role of calcium phosphate surface structure in osteogenesis and the mechanisms involved, *Acta Biomater.* 106 (2020) 22–33.
- [63] G.R. Beck, N. Knecht, Osteopontin regulation by inorganic phosphate is ERK1/2-, protein kinase C-, and proteasome-dependent, *J. Biol. Chem.* 278 (43) (2003) 41921–41929.
- [64] C. Feng, W.J. Zhang, C.J. Deng, G.L. Li, J. Chang, Z.Y. Zhang, X.Q. Jiang, C.T. Wu, 3D printing of Lotus root-like biomimetic materials for cell delivery and tissue regeneration, *Adv. Sci.* 4 (12) (2017), 1700401.
- [65] T. Li, D. Zhai, B. Ma, J.M. Xue, P.Y. Zhao, J. Chang, M. Gelinsky, C.T. Wu, 3D printing of hot dog-like biomaterials with hierarchical architecture and distinct bioactivity, *Adv. Sci.* 6 (19) (2019), 1901146.
- [66] M. Zhang, R.C. Lin, X. Wang, J.M. Xue, C.J. Deng, C. Feng, H. Zhuang, J.G. Ma, C. Qin, L. Wan, J. Chang, C.T. Wu, 3D printing of Haversian bone-mimicking scaffolds for multicellular delivery in bone regeneration, *Sci. Adv.* 6 (12) (2020) eaaz6725.